A 3D Shear Velocity Model of the Crust and Uppermost Mantle Beneath the United States from Ambient Seismic Noise

G. D. Bensen

Center for Imaging the Earth's Interior, Department of Physics, University of Colorado at Boulder, Boulder, Colorado USA

M. H. Ritzwoller

Center for Imaging the Earth's Interior, Department of Physics, University of Colorado at Boulder, Boulder, Colorado USA

Y. Yang

Center for Imaging the Earth's Interior, Department of Physics, University of Colorado at Boulder, Boulder, Colorado USA

G. D. Bensen, Department of Physics, University of Colorado at Boulder, Campus Box 390, Boulder, CO 80309, USA. (gbensen@colorado.edu)

Abstract.

Recent work in ambient noise surface wave tomography has shown that high resolution surface wave dispersion maps over large areas and across a broad frequency band can be obtained reliably in a wide variety of geographical settings. *Bensen et al.* [2007b] used 203 stations across North America to produce nearly dispersion curves for about 9,000 inter-station paths after measurement selection, creating Rayleigh and Love wave dispersion maps from 8 - 70 s period and 8 - 20 s period, respectively, on a 0.5° x 0.5° grid. These maps produce Rayleigh and Love wave group and phase speed dispersion curves at each grid node which we invert here in a two-step procedure to determine a three-dimensional (3D) shear wave velocity model of the crust and uppermost mantle beneath much of contiguous US. The first step is a linearized inversion for the best fitting model. This is followed by a Monte-Carlo inversion to estimate model uncertainty. In general, a simple model parameterization is sufficient to achieve acceptable data fit, but a Rayleigh/Love discrepancy at periods from 10 to 20 sec is observed in which a simple isotropic model systematically misfts Rayleigh and Love waves in some regions. Crustal features observed in the model include sedimentary basins such as the Anadarko, Green River, Williston Basins as well as the Great Valley and the Mississippi Embayment. The east-west velocity dichotomy between the stable eastern US and tectonically deformed western US is imaged and shown to be abrupt in the crust and uppermost mantle, but is not coincident in these regions; that is, the higher velocity material in the crust tends to lap over the higher

velocities in the uppermost mantle. Recovered crustal thickness is similar to the Crust 2.0 model of *Bassin et al.* [2000]. The Rayleigh/Love discrepancy is crustal in origin and is observed in a number of regions, particularly in extensional provinces such as the Basin and Range. It can be resolved by introducing radial anisotropy into the lower or middle crust with $Vsh > Vsv$ by about 1%.

1. Introduction

Seismic tomographic investigations on both global and regional scales have been performed in recent years covering all or part of the continental United States. However, the resulting models have had either limited geographic extent or relatively low resolution. Previous studies also have shown that surface wave ambient noise tomography (ANT) helps to fill the gap between regional and continental/global scale tomographic models (e.g., *Moschetti et al.* [2007], *Lin et al.* [2007], *Yang et al.* [2007a], *Yao et al.* [2006]). Still, the full potential of the bandwidth and, therefore, the depth extent of ANT remains untested. In addition, little work exists towards a 3D inversion of ANT results using Rayleigh and Love wave group and phase speed measurements. Employing these techniques, we show that ANT effectively diminishes the typical resolution/coverage trade-off and provides higher resolution results across the continental US than achieved by previous studies on this scale. Seismic data now emerging from Earthscope's USArray provide the potential for further improvement in resolution for which our model may serve as a useful reference.

This study is an extension of work presented by *Bensen et al.* [2007a] and *Bensen et al.* [2007b]. *Bensen et al.* [2007a] presented a technique for computing reliable empirical Green's functions (EGF) from long sequences of ambient noise. They also presented an automated procedure to measure the dispersion of EGFs as well as selection criteria to ensure that only high-quality signals are retained. Using these methods, *Bensen et al.* [2007b] estimated maps of Rayleigh and Love wave group and phase speed across the study region presented in Figure 1. Using 203 stations across North America (labeled as black triangles in Figure 1) for up to two years of ambient noise data, they developed surface wave dispersion maps across the study region on a 0.5° x 0.5° grid. They constructed dispersion maps from 8 - 70 s period for Rayleigh waves and 8 - 20 s period for Love waves. These dispersion maps form the basis for the current study. Additionally, *Bensen et al.* [2007b] presented evidence that adds further credibility to the ANT technique, as well as empirical information about the nature of the distribution of ambient seismic noise. Aspects of the work by *Bensen et al.* [2007a] and *Bensen et al.* [2007b] are summarized here as appropriate.

Regional investigations of surface wave propagation and dispersion in the United States date back over 30 years (e.g., *Lee and Solomon* [1978]). Tomographic studies using data in the United States (e.g., *Alsina et al.* [1996], *van der Lee and Nolet* [1997], *Godey et al.* [2003], *Li et al.* [2003], *Marone et al.* [2007]) created dispersion maps and models covering our study area which possess resolution similar to global scale studies (e.g., *Trampert and Woodhouse* [1996], *Ekström et al.* [1997], *Ritzwoller et al.* [2002]).

In addition, a large number of smaller-scale regional studies have been performed to investigate the seismic structure of North America. Among these are tomographic studies in regions such as the Rio Grande Rift (e.g., *Gao et al.* [2004]), Cascadia (e.g., *Ramachandran et al.* [2005]), California (e.g., *Thurber et al.* [2006]), the Rocky Mountains (e.g., *Yuan and Dueker* [2005]) and the eastern US (e.g., *van der Lee* [2002]), just to name a few recent studies among many others. Many refraction studies have provided profiles across North America, including CD-ROM (e.g., *Karlstrom et al.* [2002]), Deep Probe (e.g., *Snelson et al.* [1998]) and others. Receiver functions have provided valuable constraints on crustal thickness and structure throughout much of the continent (e.g., *Crotwell and Owens* [2005]). However, compiling and integrating regional results into a single high-resolution model with broad coverage is a difficult task considering the variety of techniques and differences in resolution and information content among them.

ANT presents several advantages over previously used techniques. First, higher seismic ray path density is achieved and these paths are contained entirely within the study region, creating a more nearly optimal configuration for tomographic inversion. Second, station locations are precisely known unlike earthquake locations. Third, new empirical observations have clarified the phase content of ambient noise for phase velocity measurements (*Lin et al.* [2007]), reducing ambiguity and facilitating high measurement precision compared to earthquake observations. Fourth, *Bensen et al.* [2007b] computed multiple, seasonally variable EGFs along each path in order to quantify measurement variability and hence uncertainty, which has been impossible with previous studies. Fifth, the bandwidth of ambient noise derived measurements (i.e., 6 - 100 s period) constrains the structure both of the crust and uppermost mantle. In contrast, it is difficult across much of the US to obtain high-quality earthquake based surface wave dispersion measurements below ∼15 s period. Despite good lateral coverage, many previous surface wave studies have obtained high-quality dispersion measurements predominantly at longer periods and, therefore, reported velocity structure only in the mantle (e.g., *Shapiro and Ritzwoller* [2002], *van der Lee and Frederiksen* [2005]). Similarly, body wave studies of similar geographic extent provide only weak constraints on crustal structure(e.g., *Grand* [1994], *Grand* [2002]). Accordingly, *Bensen et al.* [2007b] reported an increase in lateral resolution by about a factor of 5 (i.e., 200 km versus 1000 km) compared to previous earthquake based surface wave investigations of similar spatial scale.

The 3D model derived from this work will be useful to improve earthquake locations in some regions, aid receiver function studies, and provide a starting model for a wide variety of investigations across the US. This may be especially important in the context of the advancing USArray/Transportable Array experiment. Velocity models are also important tools for guiding tectonic inferences. Even by compiling multiple models one falls short of linking the unique tectonic provinces of North America into a coherent integrated model. Furthermore, less seismically active regions of North America, such as the central plains and the eastern United States, are harder to constrain seismically than the tectonically active western US. In some areas, the model presented herein will be the highest resolution model available.

The current study uses a two-step procedure to create a 1D velocity model at each point on a 0.5° x 0.5° grid across the US based on the dispersion maps of *Bensen et al.* [2007b]. The first step is a linearized inversion for an isotropic shear velocity profile from the set of dispersion curves at each grid point. The inversion is inherently non-unique and a variety of models of varying levels of complexity can be created that fit the data within the data uncertainty. In the second step of the inversion, in order to quantify the level with which we can trust the results of the inversion, we perform a Monte-Carlo resampling of model space near to the best fitting model derived from the linearized inversion, to develop an ensemble of models at each grid point that fit the data acceptably. From this we quantify the model uncertainty and choose a "favored model" near the center of the distribution to represent the ensemble. The final model is, therefore, a 3D volume of isotropic shear wave velocity and uncertainty at each point in the area of good resolution outlined with the black contour in Figure 2. The vertical extent of the model is from the surface to about 150 km depth.

2. Data

The data used in this study are the Rayleigh and Love wave group and phase speed dispersion maps from *Bensen et al.* [2007b]. These maps are based on Rayleigh and Love wave group and phase speed dispersion measurements obtained from EGFs computed along paths between the stations shown in Figure 1. Dispersion measurements are made on EGFs created by cross-correlating long ambient noise time series using the data processing and measurement techniques described in detail by *Bensen et al.* [2007a] and *Lin et al.* [2007]. Nearly 20,000 paths are used for this experiment and up to 13 unique measurements from different temporal subsets of the two-year time series along each path are computed for each wave type. An automated Frequency Time Analysis (FTAN) is necessary to measure the dispersion of these Rayleigh and Love wave signals. The seminal description of the FTAN procedure can be found in *Levshin et al.* [1972] and details of our automated procedure are outlined by *Bensen et al.* [2007a].

Bensen et al. [2007b] developed acceptance criteria to ensure that only EGFs of high quality are retained. In short, starting with nearly 20,000 paths across the United States and Canada, a maximum of 8,932 paths remained after rejection. The rejection procedure consists of three parts. The first is a minimum signal-to-noise ratio (SNR) criterion. Secondly, EGFs for different 6-month time intervals of ambient noise are computed, yielding a set of temporally variable EGFs for each path. Only observations with little variability in the repeated dispersion measurements are retained. Finally, data with large time residuals after an initial overly smooth tomographic inversion are rejected. *Bensen et al.*

[2007b] inverted the selected dispersion measurements using the tomographic method described in detail by *Barmin et al.* [2001] (an abbreviated introduction is presented by *Bensen et al.* [2007b]) to generate group and phase speed tomography maps for Rayleigh waves between 8 and 70 s period and between 8 and 20 s for Love waves. Low signal quality for Love waves at longer periods causes the narrower bandwidth and apparently results from higher local noise on horizontal components. Selected examples of these maps and discussion of their quality are presented by *Bensen et al.* [2007b]. Additionally, selected Rayleigh and Love wave group and phase speed dispersion maps can be found at *http://ciei.colorado.edu/~gbensen/dispersion_maps.html*. The resulting bandwidth presents sensitivity to shear velocity from the surface into the upper mantle, as seen in Figure 3. Our study has better shallow depth sensitivity than previous studies of similar geographic scale due to the shorter period measurements that derive from ambient noise.

Starting with the set of Rayleigh and Love wave group and phase speed dispersion maps at different periods, dispersion curves are constructed at each point on the 0.5° x 0.5° grid across the US. This process is similar to many previous studies such as *Ritzwoller and Levshin* [1998], *Villaseñor et al.* [2001], *Shapiro and Ritzwoller* [2002], *Weeraratne et al.* [2003], and others. For all periods, at each geographic point, it is important to assign an uncertainty value within which the modeled dispersion curve should lie. *Shapiro and Ritzwoller* [2002] assigned uncertainty at each point as the RMS tomography misfit weighted by resolution, which was effective for their global scale work. Given that crustal anomalies are often greater in magnitude than mantle anomalies, we favor a different approach. Changing the regularization of the tomographic inversion can affect the exact location, extent and amplitude of velocity anomalies appreciably. These changes in the recovered anomalies, due to subjective decisions, are a source of ambiguity in the tomographic results. To address this, we create a set of reasonable dispersion maps for each period and wave type by using a range of regularization parameters. The minimum and maximum velocity at each point for each period define an uncertainty window for that wave type. We find that regions of greatest variability occur near significant velocity anomalies and near the edges of the study area. We set a minimum uncertainty value for Rayleigh wave group and phase speed at 20 and 30 m/s, respectively. Love wave phase speed minimum uncertainty is set at 30 m/s. We do not use Love wave group speed dispersion curves in this study because of lower confidence in their robustness. Finally, we weight the uncertainty values by the estimated resolution. The weighting factor is unity for grid points with resolution of 400 km or better. The uncertainty at grid points with worse resolution is increased to a maximum value of 100 m/s. For reference, the 500 km resolution contour for the 16 s Rayleigh wave phase speed map is shown in Figure 2; resolution of other maps is generally no better than this. The mean uncertainty over all periods for the measurements used in this study is shown in Figure 4. Rayleigh wave uncertainty increases near the extremes of the period band. By comparison, the uncertainty values we used are smaller than RMS tomography misfit values from *Bensen et al.* [2007b] at all periods for all wave types. The uncertainties change across the US from 20 - 100 m/s for Rayleigh phase velocity maps and from 30 - 100 m/s for Rayleigh group and Love phase velocity maps.

3. Methods

Two commonly used methods exist for estimating shear wave velocity structure from surface wave dispersion measurements. The first is linearized waveform fitting as described by *Snieder* [1988], *Nolet* [1990] and others. This technique has been used in many geographical settings with earthquake surface wave signals, including the US (*van der Lee and Nolet* [1997]). The second method, which we adopt, is a two-stage procedure in which period specific 2D tomographic maps created from the dispersion measurements first are used to produce dispersion curves at each geographic grid point. The dispersion curves are then inverted for 1D *Vs* structure at all grid points and the 1D models are compiled to obtain a 3D volume. This procedure has been described by *Shapiro and Ritzwoller* [2002] and elsewhere.

Out specific approach to the second stage of inversion divides into two further steps. The first step is a linearized inversion of the dispersion curves for the 1D velocity structure at each point based on the method of *Yang and Forsyth* [2006]. However, the best fitting model does not account for the non-uniqueness of the inverse problem; a variety of acceptable models may be created that fit the data with the desired accuracy. In the second step, for this reason, we perform a Monte-Carlo search of a corridor of model space defined by the results of the linearized inversion. From this we define an ensemble of velocity models that fit the data acceptably. In contrast, a Monte-Carlo search of a broader model space, which is not constrained by the results of the linearized inversion, is much slower. These two steps are outlined further below. The linearized inversion procedure only uses Rayleigh and Love wave phase speed measurements while Rayleigh wave group speed measurements are also included in the Monte-Carlo procedure.

3.1. Starting Models and Parameterization

Both the linearized inversion and the Monte-Carlo resampling require a starting model. Previous work used AK135 (*Kennett et al.* [1995]) as a starting model for all points (e.g., *Weeraratne et al.* [2003]; *Yang and Forsyth* [2006]). For the linearized inversion, we observe faster and more stable convergence by using unique starting models at each geographic point. For this purpose, we extract shear wave speed values from the 3D model of *Shapiro and Ritzwoller* [2002]. The procedure also requires values of P-wave speed (Vp) and density (ρ). We use the average continental Vp/Vs ratios of 1.735 in the crust and 1.756 in the mantle from *Chulick and Mooney* [2002] who found little deviation from these values across the US. Furthermore, surface waves are less sensitive to Vp than Vs except in the uppermost crust. Density (ρ) is assigned similarly using a ρ/Vs ratio of 0.81 as described by *Christensen and Mooney* [1995]. Following previous work (i.e., *Weeraratne et al.* [2003]; *Yang and Forsyth* [2006]), we parameterize the models with 18 layers. Three crustal layers are used where the top layer thickness is set at the greater of 2 km or the sediment thickness from the model of *Laske and Masters* [1997]. The depth to the Moho was extracted from *Bassin et al.* [2000]. These two inputs define a thin upper crustal layer and a thick middle to lower crustal layer. The lower crustal layer was separated into two layers of equal thickness defining the middle and lower crust. The 15 layers in the mantle are between 20 and 50 km thick and extend to 410 km depth. An illustration of the parameterization is shown in Figure 5a. In the linearized inversion, the velocities of all layers are allowed to change although regularization is applied to ensure smoothness, as discussed in Section 3.2 below. Vp/Vs and ρ/Vs are maintained at the values stated above. Finally, only the thicknesses of the lower crust and uppermost mantle are permitted to change. However, if poor data fit is observed, we perturb the upper and middle crustal layer thicknesses (while maintaining the initial crustal thickness) and the inversion is rerun.

For Monte-Carlo sampling we use the result of the linearized inversion as a starting model. However, we also impose an explicit requirement of monotonically increasing crustal velocity with depth. Within our study area, *Wilson et al.* [2003] and *Ozalaybey et al.* [1997] found evidence for a low-velocity zone (LVZ) in the crust from localized magma bodies and regional partial melt, respectively. Using receiver functions and surface wave dispersion to constrain the crust, *Ozalaybey et al.* [1997] allowed ∼20 crustal layers. At a variety of locations, their crustal LVZ was often 5 km or less in thickness. These crustal LVZs and other similar features documented in the literature are of insufficient vertical and/or lateral extent for us to image reliably. Furthermore, a model parameterization using isotropic crustal velocities still produces fairly good data fit in most cases. In contrast, *Ozalaybey et al.* [1997] find evidence for an upper mantle LVZ in northwestern Nevada, which is permitted in our mantle parameterization. In the mantle, Monte-Carlo sampling of 15 layers, as used in the linearized inversion, is costly and would potentially create unrealistic models or require the additional complexity of a smoothing regularization. For speed and smoothness, we parameterize the mantle with five B-splines. An illustration of this parameterization of the model is shown in Figure 5b.

From the linearized inversion described above, we obtain smooth, simple 1D velocity profiles at all grid points in the study area which typically fit the data remarkably well. For the Monte-Carlo sampling we define the allowed range of models based on this best fitting result. First, we impose a constraint on the permitted excursions from the initial velocity values. The velocity must be within ± 20% of the initial model in the upper crust and ± 10% in the lower crust and mantle. We choose this range rather than a specific velocity window (e.g., ± 0.5 km/s) because of the potential for unrealistically low values in the crust. By comparison, our allowed corridor is wider than that of *Shapiro and Ritzwoller* [2002]. Again, we maintain the Vp/Vs and Vs/ρ values stated above. However, the thicknesses of the crustal layers can now vary while the sum of crustal layers must be within $\pm$ 5 km from the Crust 2.0 model of *Bassin et al.* [2000].

Complexities probably exist within the crust and upper mantle that may not be well represented by our simple parameterization. However, if data fit is reasonable, we cannot empirically justify a more complicated model without inclusion of independent information such as receiver functions. The non-uniform coverage of receiver functions would make this particular exercise difficult on our scale at this time.

3.2. Linearized Inversion

The linearized inversion process uses the starting model described in section 3.1 to create predicted dispersion curves. Perturbing the input model provides misfit information and iterating converges upon the best-fitting solution. The linearized inversion process follows the work of *Li et al.* [2003], *Weeraratne et al.* [2003], *Forsyth and Li* [2005], *Yang and Forsyth* [2006] and others. In this case, the forward code used to compute dispersion curves from an input model is based on *Saito* [1988].

The technique to find the best fitting velocity model is outlined by *Weeraratne et al.* [2003] and is based on the iterative least-squares approach of *Tarantola and Valette* [1982]. *Li et al.* [2003] concisely summarize the approach, which we excerpt here. The solution is described by the equation:

$$\mathbf{\Delta m} = (\mathbf{G}^T\mathbf{C}_{nn}^{-1}\mathbf{G} + \mathbf{C}_{mm}^{-1})^{-1}(\mathbf{G}^T\mathbf{C}_{nn}^{-1}\mathbf{\Delta d} - \mathbf{C}_{mm}^{-1}[\mathbf{m} - \mathbf{m_0}]) \quad (1)$$

where $\mathbf{m}$ is the current model, $\mathbf{m_0}$ is the starting model at the outset of each iteration, and $\mathbf{\Delta m}$ is the change to the model. $\mathbf{\Delta d}$ is the difference between the observed and predicted data. $\mathbf{G}$ is a sensitivity matrix relating changes in $\mathbf{d}$ to changes in $\mathbf{m}$. $\mathbf{C}_{mm}$ is the model covariance matrix where non-zero values (we use 0.1) are introduced into the off-diagonal terms in order to provide a degree of correlation between velocity values obtained for adjacent layers and ensure a reasonable model (i.e., a model without large velocity jumps or oscillations). $\mathbf{C}_{nn}$ is the diagonal data covariance matrix where the diagonal elements are calculated from the standard errors of the phase velocities.

As a measure of data fit quality, we use reduced χ^2 (henceforth χ^2). Unique χ^2 values are computed for Rayleigh wave and Love wave phase speed; χ^2 is also computed for Rayleigh wave group speed in the Monte-Carlo resampling described below. χ^2 is defined as

$$\chi^2 = \frac{1}{n}\sum_{i=1}^{n}\frac{(\tilde{d}_i - d_i)^2}{\delta_i^2} \tag{2}$$

where i is the index of the period of the measurement through all wave types used. Periods used are on a 2 second grid from 8 - 20 s period and every 5 seconds for 25 - 70 s period. Therefore, n is 7 for Love waves and 17 for Rayleigh waves. Thus, in the linearized inversion, 24 measurements are used but in the Monte-Carlo inversion, 41 measurements are applied because Rayleigh wave group speeds are utilized. $\tilde{d}$ and d_i are the model predicted and measured wave speeds, respectively, and δ_i is the uncertainty of the measured velocity unique to each period, wave type, and location, as described in Section 2 above. χ^2 is a measure of how well the model prediction fits the data within estimated uncertainty values. A χ^2 value less than or equal to unity indicates a fit within the estimated uncertainty of the data. Generally, χ^2 values of 2 or less represent fairly good data fit, although misfit systematics may still exist for χ^2 ranging from 1.5 to 2. Higher values indicate inferior fit or underestimated data uncertainties.

An example of input data and model output from the linearized inversion is shown in Figure 6 for a point in Illinois. For reference, the location of this point is plotted as a grey circle in Figure 1. Dispersion observations and associated errors are plotted as error bars in Figure 6a. The resulting best fitting model and related dispersion curves produced by linearized inversion are shown as thin black lines in Figure 6. For comparison, the starting model and the related dispersion curves are shown in Figure 6 as dotted grey lines.

Variability in data fit quality is present in the study area. Figure 7 shows two more examples like Figure 6 but with higher resulting χ^2 values. Considering that the location of data used in Figure 7c,d is in an area of particularly good resolution (southern California), the misfit most likely derives from improper model parameterization. In this case, the short period under-prediction of Love wave speeds and over-prediction of Rayleigh wave speeds may indicate the need for radial anisotropy in the crust. More discussion of alternative parameterizations follows in Section 6.3. For reference, the approximate depth sensitivities of Rayleigh and Love phase velocity at selected periods are shown in Figure 3. Examination of these sensitivity plots confirms that higher misfit (e.g., Figure 7a,c) could be due to improper model parameterization at depths from 0 - 30 km.

3.3. Monte-Carlo Resampling and Uncertainty Estimation

To estimate uncertainties in geophysical inverse problems, model space sampling method such as Monte-Carlo methods have been in use for over 40 years (*Keilis-Borok and Yanovskaya* [1967]) and can provide reliable uncertainty estimates even when the *a priori* probability density of solutions is unknown (see *Mosegaard and Tarantola* [1995]).

Variations among Monte-Carlo methods are summarized by *Sambridge and Mosegaard* [2002]. Methods to sample model space more effectively and/or more quickly are presented therein. One particular concern in our inverse problem is the tradeoff between velocity values in the lower crust and uppermost mantle with crustal thickness. This is considered a significant problem by *Marone and Romanowicz* [2007] and elsewhere and provides part of the motivation for us to estimate model uncertainty. We quantify the variation of acceptable models and use this variation as an indication of the robustness of the resulting velocity model.

Our Monte-Carlo procedure is a two-step process that first creates models through uniformly distributed random perturbations within the permitted corridor around the model provided by linearized inversion, as described above. Secondly, a random walk is used to refine the search for acceptable models. Rayleigh wave group and phase and Love wave phase speed dispersion curves are generated for each model using the forward code of *Herrmann* [1987]. If the predicted dispersion curves match the measured results at an acceptable level, the model is retained. An acceptable model is defined as one having a χ^2 value within 3 times the χ^2 value obtained from the linearized inversion. For Rayleigh wave group velocity values, the χ^2 limit is 6 times the Rayleigh wave phase velocity best fit value. Fairly conservative error estimates result from these choices. In order to accelerate the process of obtaining a sufficient number of acceptable models, the random walk procedure generates small perturbations to search adjacent model space for additional acceptable models. After the random walk identifies an acceptable model, the search re-initializes in the neighborhood of that model until we construct 100 acceptable models. This number of models is arbitrary, but appears to be large enough to quantify model uncertainty to form the basis for our inferences and is computationally tractable.

An example of the observed dispersion curves and the Monte-Carlo results are shown in Figure 8 for points labeled as grey squares in Figure 1. The model ensembles in these examples display the strongest variability at different depths while all have similar variability in the resulting dispersion curves. Thus, the goodness-of-fit for a computed dispersion curve is not necessarily a clear indicator of a robust model.

We select a "favored model" from the set of resulting velocity models. The best-fitting model is very similar to that determined through linearized inversion and may not represent the ensemble of models very well. We favor the model closest to the mean of the distribution, where greater depths are given lesser precedence. This captures the essence of the ensemble and diminishes the occasional problems of lateral roughness found when only the best fitting velocity models are considered. For illustration, the models identified as most near the mean of the distribution are plotted in red in Figure 8a,c,e and are, henceforth, referred to as the "favored models". Further discussion of model variability across the study area is reserved for Section 5 below.

4. Crustal Rayleigh/Love Wave Speed Discrepancy

The observation of relatively poor data fit in regions of good resolution deserves further comment. The distributions of χ^2 values for Rayleigh and Love wave phase speeds separately are shown in Figure 9. Because the inversion procedure attempts to minimize data misfit for Rayleigh and Love waves simultaneously, the observation that areas of high χ^2 for Rayleigh and Love waves approximately coincide is no surprise. The primary cause for larger misfit may be attributed to three factors. The first factor is that the data error estimates that we used could be too low in some regions where our confidence in the input dispersion maps is overestimated. This may be the case along the edges of the study region. Secondly, higher misfit may also occur when the results for different wave types have incompatible resolutions causing velocity transitions to manifest themselves in different locations for different wave types. The third factor is that our simple model parameterization insufficiently describes the earth at a given point. Poorer agreement in the data primarily at short periods suggests that the deficiency in parameterization would be in the crust.

A three-layer crust and multi-layer mantle can usually fit either Rayleigh or Love wave measurements satisfactorily. However, fitting data to both simultaneously is more difficult. Figure 10 shows the difference in misfit to Rayleigh and Love waves phase velocities across the US where, unlike χ^2, the sign of the misfit is retained. We compute the dispersion predicted by the "favored model" minus the observed dispersion at each geographical point and divide this by the estimated data error. These values are averaged from 8 - 20 s period. Green and orange colors signify that the model is faster than an observation at a point. Blue colors indicate that the model is too slow to fit the observations. The widespread result of Rayleigh and Love wave speeds being over- and under-predicted, respectively, is apparent. The period band (8 - 20 s) indicates that the source of this discrepancy lies in the crust. We, therefore, refer to this as the crustal Rayleigh/Love discrepancy to distinguish it from the well known mantle Rayleigh/Love discrepancy caused by radial anisotropy due to olivine alignment in the mantle (e.g., *Dziewonski and Anderson* [1981]). Section 6.3 below discusses possible causes of this observation and our preferred explanation.

5. Results

We construct a "favored model" from an ensemble of models that fit the data acceptably developed through Monte-Carlo inversion at each grid point. Combining these 1D isotropic models, we obtain a 3D shear wave velocity model for the continental US with lateral coverage bounded approximately by the black contour in Figure 2 and depth range from the surface to 150 km. Here, we characterize the model by highlighting examples of the types of features it contains. The names of features listed in Figure 2 are used in this discussion.

Horizontal slices of isotropic shear wave speed at a selection of depths are shown in Figure 11 including 4 km above (Figure 11c) and 4 km below (Figure 11d) the recovered Moho. For plotting purposes, we smooth the model features and soften the abrupt contrasts between layers, by vertically averaging in 4 km increments in the crust and 10 km in the mantle. Thus, a depth section at 10 km is the average from 8 - 12 km depth. No smoothing is applied across the Moho.

The most striking features at 4 km depth (Figure 11a) are several large sedimentary basins. The Mississippi Embayment and the Green River Basin appear most strongly. Additionally, the Williston Basin and Anadarko Basin in Montana and Oklahoma, respectively, clearly appear as slow velocity anomalies. Low velocities associated with the sediments of the Great Valley in California abut slow crustal velocities of the Cenozoic Pacific Northwest volcanic province farther north. A trend of generally faster velocities in the eastern US compared with the western US is also observed.

At a depth of 10 km (Figure 11b), the most pronounced feature is again the strong signal from the deep sediments of the Mississippi Embayment, which has been extended to this depth by the vertical averaging. The crustal velocity "dichotomy" observed at 4 km depth between the faster eastern US and slower western US continues to be clearly defined. The crustal velocity dichotomy at this depth is located along the boundary between the Great Plains and Central Lowlands and will be discussed in detail in Section 6.1 below.

Moving to the lower crust, Figure 11c at 4 km above the Moho shows a different location of the crustal velocity dichotomy in the central US, shifted west to coincide with the transition from the Great Plains to the Rocky Mountain Front. Also, the slow anomaly in the Basin and Range can be attributed to high crustal temperatures in this extensional province, as evidenced by high surface heat flow in the area (see e.g., *Blackwell et al.* [1990]). The fast anomaly in the Great Lakes area may result from regionally thicker crust; a slice at 4 km above the Moho is at a greater depth than the surrounding region. However, slower speeds beneath the Appalachian Highlands to the east is within similarly thick crust, implying that compositional differences between the Appalachian Highlands and the continental shield are the more likely cause of this velocity anomaly. For reference, the estimated crustal thickness is shown in Figure 12 and is discussed below.

At 4 km below the Moho (Figure 11d), the east-west velocity dichotomy is in a similar but not identical location as in the lower crust. This will be discussed at greater length in Section 6.1 below. East of this transition, more laterally homogeneous mantle velocities appear. To the west, the prominent slow anomaly below the eastern Basin and Range is striking and corroborates the suggested removal of mantle lithosphere from 10 Ma to present (e.g., *Jones et al.* [1994]) and replacement with warmer, low velocity mantle material. The slow anomaly in the Pacific Northwest can be attributed to the volatilized mantle wedge residing above the subducting slab. At 80 km depth (Figure 11e), however, the slow anomaly associated with the mantle wedge is no longer visible, suggesting that this depth is below or within the subducting slab. Also, a slow mantle velocity anomaly extends in the northwest to southeast direction, roughly following the outline of the entire Basin and Range province. A similar feature was also observed in the tomographic models of *Alsina et al.* [1996] and others and has been attributed to inflow of warm mantle material during Cenozoic extension (e.g., *Wernicke et al.* [1988]). At 120 km depth in Figure 11f, features are similar to 80 km depth, but anomalies are of lower amplitude.

The estimated crustal thickness is similar to the starting model of Crust 2.0 (*Bassin et al.* [2000]) and is shown in Figure 12. On average, the crust is 1.6 km thinner than Crust 2.0 and the RMS difference from Crust 2.0 across the study region is 1.5 km. These differences are not strongly concentrated in any specific regions where the Monte-Carlo ensemble suggests a significant offset from the Crust 2.0. The relation of crustal thickness with topography and implications for topographic support or compensation are discussed later in this section.

Vertical cross-sections through the velocity model on a 0.5° grid reveal more information about structures within the study area. Figure 13 presents a series of vertical cross-sections with locations indicated on the map in Figure 13a. A smoothed elevation profile is plotted above each cross-section and a profile of the recovered crustal thickness is overplotted. We use different color scales for crustal and mantle shear wave speeds. To diminish the appearance of small lateral differences as vertical stripes, smoothing has been applied for plotting purposes by averaging velocity values at each depth with those of neighboring horizontal grid points in the crust and mantle. Crustal structure is smoothed by taking a weighted average that includes the four nearest grid points in map view. Mantle structure is similarly smoothed, but the weighted average includes the eight nearest grid points. Vertical smoothing is also used as described above in the discussion of Figure 11. The vertical exaggeration of the cross-sections is roughly 25:1 and the same horizontal scale is used for N-S and E-W cross-sections.

As with the horizontal depth-sections presented in Figure 11, the most pronounced shallow crustal velocity anomalies are from sedimentary basins, although vertical smoothing extends these features to greater depths. Profiles C-C' and F-F', for example, show that the sediments of the Mississippi Embayment extends inland from the coast for hundreds of kilometers. The most pronounced velocity contrasts result from the location of the east-west velocity dichotomy in the crust and upper mantle, as will be discussed in more detail in Section 6.1 below. Slow mantle velocities exist from the Rocky Mountains to the west and are particularly low in the Basin and Range, which has been altered by extension. A discussion of the amplitude of observed mantle anomalies compared to previous work is presented in Section 6.2 below.

The relation between surface topography, crustal thickness, and crust and mantle velocities allows qualitative conclusions to be drawn regarding the support for high topography in the US. In general, surface topography within the US is not well correlated with crustal thickness. For example, the north-south profiles in Figure 11 reveal very little relation between the surface and Moho topography. Profile E-E', in particular, reveals crustal thickness to be anti-correlated with topography and substantial Moho topography exists under regions with almost no surface topography in Profiles F-F' and G-G'. In addition, the Basin and Range province is characterized by high elevations, but the crust is relatively thin. In all of these areas, however, high elevations with relatively thin crust are underlain by a slower and presumably less dense crust and mantle, indicative of a Pratt-type of compensation or dynamical support for the topography. There are exceptions, however. Running from west to east along Profile B-B', the highest elevations coincide with a mantle that is relatively slow and the crust is thick. Farther east in the Great Plains, the thinning crust and decreasing elevation are coincident, suggesting an Airy-type of compensation.

The standard deviation (σ) of the ensemble of Monte-Carlo models computed at each grid point indicates the confidence in the velocity values through depth and across the study region. Average values for σ versus depth are shown in Figure 14a. Except near the surface, the average value of uncertainty is about 1.5% with this value increasing slightly with depth. The RMS of velocities as a function of depth taken over the entire region of study is also shown in Figure 14 to be about 3%, except near the surface. Thus, lateral velocity anomalies are, on average, about twice the size of the uncertainties. The lower anomaly values observed in the middle crust are likely because topography is not allowed on the layer boundaries above and below to tradeoff with it, leading to a lower ensemble standard deviation. The jump in RMS anomaly values near 40 km depth is caused by laterally averaging both crust and mantle velocities. Figure 15 shows the amplitude and distribution of σ across the study region at the depths presented in Figure 11. At 4 km depth, σ is greatest near the edges of the study area, in part due to higher expected data errors caused by lower resolution. Low σ values at 10 km depth (Figure 15b) through much of the study region, as mentioned above, are due to the lack of boundaries above and below this layer with which to trade-off. A parameterization that allows topography or more crustal layers would generate greater middle crustal σ values. In the lower crust

(Figure 15c), σ is greater than in the mid-crust due to the tradeoff between wave speed and crustal thickness; similar values are observed in the upper mantle (Figure 15d) due to the same tradeoff. At 80 km (Figure 15e), σ is lower than at shallower depths and is more uniform. The uniformity extends to 120 km depth (Figure 15f), although the amplitude of σ increases slightly at this depth due to poorer sensitivity at greater depths as indicated in Figure 3.

Figure 14b shows the average standard deviation in the dispersion curves produced by the ensemble of acceptable models. Greater variability in model velocity values in the uppermost crustal layer results in the higher standard deviation values at short periods (i.e., < 15 s period). Rayleigh and Love wave phase speed variability is nearly constant at 0.5% while the Rayleigh wave group speed variability is higher due to the higher χ^2 misfit threshold used in the Monte-Carlo resampling.

6. Discussion

A detailed interpretation of the estimated 3D model is beyond the scope of this paper. We discuss three specific questions and emphasize using the model uncertainties to address them. First, we constrain the location of the east/west velocity dichotomy in the lower crust and uppermost mantle. Second, we compare the amplitude of the observed mantle velocity anomalies to those of the global model of *Shapiro and Ritzwoller* [2002]. Finally, we present alternative model parameterizations in the attempt to resolve the crustal Rayleigh/Love velocity discrepancy discussed in Section 4 above.

6.1. East-West Shear Velocity Dichotomy

The difference in crustal and uppermost mantle shear wave speeds between the faster tectonically stable eastern US and the slower tectonically active western US is visible in the horizontal and vertical cross-sections presented in Figures 11 and 13. This is also a feature of older tomographic models. Here, we use the ensemble of models from the Monte-Carlo inversion to estimate the location of and uncertainty in this velocity dichotomy.

First, Figure 16 presents histograms of velocity values along 40°N within the eastern and western US for the lower crust and at 80 km depth. The values are taken from our favored model from the Monte Carlo inversion. The eastern and western US are separated approximately by a shear velocity of about 3.75 km/sec in the lower crust and 4.55 km/sec in the uppermost mantle, but the exact choice of these values affects our conclusions only slightly. Note first that the two distributions are nearly disjoint, indicating a strong compositional and/or thermal difference between the tectonically active western US and the stable eastern US. Secondly, the distribution in the eastern US is somewhat tighter, particularly in the lower crust, demonstrating that the eastern US is somewhat more homogeneous than the west.

To determine the location of the boundary of the east-west dichotomy, shear velocity values for the lower crust and at 80 km depth are sorted and ranked by V_s value for the ensemble of 100 acceptable models produced by the Monte Carlo inversion at each grid point. In Figure 17, contours are plotted through the 20th and 80th maps (which can be thought of as the 20th and 80th percentile values within the ensemble of accepted models at each point) for values of 3.75 km/s in the lower crust and 4.55 km/s at 80 km depth as grey and blue lines, respectively. The separation between the tectonically active western US and the stable eastern US lies approximately between these contours.

In the lower crust (Figure 17a), the western velocity contrast roughly follows the Rocky Mountain Front from Wyoming to the south, but veers to the west north of central Wyoming, crossing the Rocky Mountain front. This east-west contrast occurs abruptly. In fact, examining the lower crustal velocity values across a variety of latitudes, a velocity change of roughly 300 m/s typically occurs over less than 100 km laterally. Both the 20th and 80th percentile values are seen in the western US. In the eastern US, the 20th percentile contour outlines the southeastern edge between the North American craton and the Appalachian Highlands farther east. This velocity contour does not precisely follow the western edge of the Appalachian highlands as plotted in Figure 2, which may be due to the lower resolution in the eastern US. The Mid-Continental Rift (MCR), oriented in a NNE-SSW direction in the central US, is also apparent. This feature is subtle in velocity depth- and cross-sections but clearly appears here, with a location that agrees with the configuration apparent in gravity maps.

At 80 km depth in the mantle, a similar set of contours outlines the eastern edge of the slower western US. However, the location of these contours now aligns better with the Rocky Mountain Front in the northern part of the study area and lies farther east in the southern portions. The eastern contour provides an outline of the cratonic lithosphere.

In summary, the range of locations is sufficiently narrow to constrain the boundary of the dichotomy in the lower crust and uppermost mantle and to observe that these locations are similar but not identical. First, the fact that slower and presumably less dense mantle material often extends well east of the Rocky Mountain Front suggests that mantle compensation plays a role in the high topography of that region. Second, the dichotomy boundary in the lower crust lies west of the mantle boundary in the western US.

Assuming that this boundary marks the approximate edge of the craton, this means that the cratonic crust extends out farther from the interior of the craton than the cratonic mantle. This apparent overhanging of the cratonic crust may be caused by mantle lithospheric erosion due to small-scale convection. Third, the lower crustal boundary crosses the Rocky Mountain front, probably reflective of crustal deformation beneath and west of the northern Rocky Mountains.

6.2. Comparison with a Global Scale Model

A comparison with previous global tomography models identifies the effect of the improved resolution of this study. Resolution has been improved both vertically and laterally. Improved vertical resolution results from the fact that ambient noise EGFs permit much shorter period dispersion measurements. Improved lateral resolution results from the inter-station dispersion measurements being made over a shorter distance than teleseismic observations. Figure 18a shows a cross section from the model of *Shapiro and Ritzwoller* [2002] compared to our result (Figure 13, $\mathbf{B}-\mathbf{B}'$) at 40°N (see location in Figure 13a). For reference, the difference is plotted in Figure 18b. The primary differences are in the mantle, but some of the crustal differences highlight the better crustal resolution afforded by ambient noise tomography. For example, the slower velocities in the upper crust beneath the Basin in Range seen in Figure 13 and the correlation of these low velocities with high topography illustrates the higher resolution. More significantly, the amplitudes of the mantle velocity anomalies in the global model are much larger than those revealed by ambient noise. Considering the full range of models in our Monte-Carlo ensemble we find that the lower range of values in the slow mantle anomaly between 245° and 250°E in profile $\mathbf{B}-\mathbf{B}'$ is roughly 4.2 km/s, which is higher than the 4.1 km/s seen in Figure 18a. However, the fast end of the model ensemble for mantle velocities between 255° and 265°E is roughly 4.65 km/s which is less than the 4.75 km/s observed in the same region by *Shapiro and Ritzwoller* [2002].

The model of *Shapiro and Ritzwoller* [2002] was created using diffraction tomography, with broad finite frequency sensitivity kernels. *Ritzwoller et al.* [2002] assessed differences in the results between ray theoretical and diffraction tomography and showed that finite frequency kernels systematically produce higher anomaly amplitudes. We attribute the differences observed between Figures 13 ($\mathbf{B}-\mathbf{B}'$) and Figure 18a to the effects of finite frequency tomography at teleseismic distances overestimating anomaly amplitudes. This provides evidence that the effective width of the sensitivity kernels for finite frequency tomography should be much narrower than the full sensitivity kernel, and closer to ray theory. It also highlights the general problem of estimating amplitudes accurately using single-station teleseismic methods.

6.3. Resolving the Crustal Rayleigh/Love Wave Speed Discrepancy

Section 4 documents the systematic misfit of Rayleigh and Love wave phase velocities below about 20 sec period by a simple isotropic parameterization of the crust with monotonically increasing velocities with depth. Figure 10 presents a summary that shows that, on average, Rayleigh wave speeds are overpredicted and Love wave speeds are underpredicted by the isotropic model that aims to fit both simultaneously. Figure 19a shows an example inversion for a point in northwest Utah (located with a grey star in Figure 1) illuminating how the estimated isotropic model (red line) predicts Love wave speeds that are too slow and Rayleigh wave speeds that are too fast, particularly below about 15 sec period. Apparently, the model parameterization is inadequate to fit both types of data simultaneously. The most likely cause of the problem is either the constraint that imposes vertical monotonicity within the crust or the fact that only isotropic models are constructed within the crust. We test both alternatives.

To determine whether crustal radial anisotropy can resolve the short period Rayleigh-Love discrepancy, we allow only the middle crust to be radially anisotropic. The rest of the model is fixed on the ensemble of isotropic profiles determined from the Monte-Carlo inversion. We perform a grid search over small perturbations in Vs in the middle crust ($\pm$500 m/s) which attempts to fit the Rayleigh and Love wave phase velocity measurements below 25 sec separately. In the inversion with the Rayleigh wave data alone we recover a set of allowed Vsv values in the middle crust and with the Love wave data we get a set of allowed Vsh values. The model is isotropic outside the middle crust. The result for the best fitting radially anisotropic model for the point in northwest Utah is shown in Figure 19a (blue line). The model itself with bifurcated Vsh and Vsv values is shown in Figure 19b where blues denote Vsv and reds denote Vsh in the middle crust and the model outside the middle crust is isotropic ($Vsh = Vsv = V_s$). In general, allowing radial anisotropy in the middle crust can resolve the Rayleigh - Love discrepancy. We have also performed the experiment allowing lower crustal radial anisotropy, but on average it does not fit the data as well as middle crustal anisotropy alone. A combination of middle and lower crustal radial anisotropy cannot be ruled out, however.

Although Love waves are predominantly sensitive to Vsh and Rayleigh waves to Vsv, there is weak sensitivity of each wave type to the alternate shear wave speed. Thus, separately inverting Love and Rayleigh waves for Vsh and Vsv, respectively, is not fully accurate. To test the approximation, we performed tests using the anisotropic "MINEOS" code of *Masters et al.* [2007]. We created synthetic dispersion curves from models possessing radial anisotropy in the crust and then inverted them to estimate the anisotropy using the procedure outlined above. The approximation we apply recovers the initial model to within about 5 m/s (∼0.1%), which is an order of magnitude smaller than the amplitude of the dispersion signals that are attempting to explain. The approximation that we use, therefore, is more than accurate enough for the inferences drawn here.

We have also investigated whether breaking the monotonicity constraint can resolve the Rayleigh - Love discrepancy. An example inversion in which a fourth crustal layer has been introduced and the monotonicity constraint has been broken is shown with the green lines in Figure 19. In this case a low velocity zone (LVZ) is introduced in the lower crust. Breaking the monotonicity constraint and introducing another crustal layer improves the fit to the data, but does not resolve the discrepancy as well as allowing a single middle crustal anisotropic layer. We extended this test across all of Nevada where radial anisotropy improves data fit and where crustal low velocity zones have been previously documented. *Ozalaybey et al.* [1997] found thin crustal LVZs (∼5 km thick) at points in this area using a joint receiver function/surface wave technique. For the 93 grid points tested, our procedure was not able to obtain the quality of fit observed using radial anisotropy, as the misfit results in Table 1 show. The values contained within the table are averaged over dispersion measurements from 10 to 20 sec period. We find that the χ^2 misfit with the radially anisotropic crust across Nevada is 1.06, yielding $\sim 42\%$ variance reduction compared to the isotropic model with monotonically increasing shear wave speeds. This means that the data are fit, on average, to within the measurement errors and no misfit systematics are observed. The non-monotonic isotropic model gives only a

15% variance reduction, but a χ^2 value of 1.54, which indicates that the measurements are misfit at the level of 1.5 measurement errors, on average, and misfit systematics continue in evidence. Breaking the monotonicity constraint and adding a single crustal layer, therefore, does not allow the data to be as fit well as by radial anisotropy. The introduction of more crustal layers and the development of more complicated models cannot be formally ruled out as an alternative, but the layerization will have to be extensive and complicated.

Thus, the introduction of radial anisotropy to the model parameterization is most effective at resolving the discrepancy and we believe radial anisotropy is the most likely physical cause. The mapping of radial anisotropy in the upper mantle using fundamental mode Rayleigh and Love waves is a well established technique (e.g., *Tanimoto and Anderson* [1984], *Montagner* [1991]). *Shapiro et al.* [2004] used shorter period Rayleigh and Love wave observations to constrain radial anisotropy in the Tibetan crust, which they attributed to crystal alignment caused by crustal flow. The widespread search for crustal radial anisotropy has been hindered by a lack of short period dispersion observations (below 20 sec period) over extended regions, which ambient noise tomography now provides.

Figure 20a presents the middle crustal radial anisotropy for the best fitting radially anisotropic model, where green and orange colors indicate positive anisotropy ($Vsh > Vsv$) and blue colors indicate the reverse. In this compilation, most of the US has radial anisotropy above the level of $\pm 1\%$ and most areas have positive anisotropy. This does not mean, however, that the anisotropy is required to fit the data. To determine this we present in Figure 20b the model with the minimal anisotropy that fits the data acceptably.

In this result, the middle crust across much of the US is white (i.e., isotropic) and the regions with negative anisotropy largely disappear.

There remain in Figure 20b several regions in which radial anisotropy in the middle crust is required to fit the data. These regions tend to be of two main tectonic types: sedimentary basins and extensional regions. The Anadarko (western Oklahoma), Appalachian, and Green River (western Wyoming) basins are clearly outlined. In these cases, layering of sediments may cause different *Vsh* and *Vsv* values in the uppermost crust and some improvement in data fit is observed by allowing radial anisotropy in the middle crust. These features may be artifacts, however, caused by poor parameterization of the vertical V_s velocity gradient in the sediments or perhaps by the strong lateral contrast across which the Love and Rayleigh waves sample differently (e.g., *Levshin and Ratnikova* [1984]). Radial anisotropy at about 2 - 4 % is observed through much of the Basin and Range, extending southeast toward the Rio Grande Rift. The observed radial anisotropy may be due to crystalline reorganization effected during Cenozoic extension. *Shapiro et al.* [2004] attributed observed radial anisotropy to the alignment of mica crystals in the crust. The effects of other compositional organizations, such as aligned cracks (e.g., *Crampin and Peacock* [2005]) or layering (e.g., *Crampin* [1970]), have also been shown to cause seismic anisotropy. The multiplicity of sources of radial anisotropy must be considered when interpreting these results.

Presentation of the 3D distribution of *Vsh* and *Vsv* and further investigation of alternative parameterizations and physical causes awaits more exhaustive studies based on the USArray/Transportable Array.

7. Conclusions

We present a 3D shear velocity model of the crust and uppermost mantle beneath much of the continental United States. The model is constrained by Rayleigh group and phase velocity measurements from 8 to 70 s period and Love wave phase velocities from 8 to 20 s, both determined by ambient noise tomography (ANT) presented previously by *Bensen et al.* [2007b]. We employ a two-step procedure to obtain shear wave speeds in the crust and uppermost mantle from the surface to approximately 150 km depth. In the first step, a linearized inversion is performed to find the best fitting model at each grid point on a 0.5° x 0.5° grid across the US. This is followed in the second step by a Monte-Carlo inversion to estimate the ensemble of models that fit the data acceptably and, hence, to bound model uncertainties.

The 3D model presented here displays higher resolution than earlier models produced using teleseismic earthquake data on a similar scale. The amplitude of features in the model, however, tends to be muted relative to global models such as that of *Shapiro and Ritzwoller* [2002]. We believe this is due to the tendency for large-scale inversions to over-estimate anomaly amplitudes perhaps indicating that the finite frequency kernels used by *Shapiro and Ritzwoller* [2002] were too broad. At the largest scales, the outline of the structural dichotomy between the tectonic west and the stable eastern part of the US is clearly defined in both the crust and uppermost mantle and is observed to be very abrupt. The location of the transition between the tectonic and stable regions is shown to be similar in the lower crust and uppermost mantle, but not coincident. In the western US, high velocities in the crust typically extend further to the west than in the mantle, particularly north of Colorado. On smaller scales, numerous intriguing features within the model are imaged, such as sedimentary basins in the shallow crust, the indication of the mid-continental rift in the lower crust, and the generally variable correlation between surface and Moho topography across much of the country. The estimated crustal thickness is similar to model Crust 2.0 of *Bassin et al.* [2000] across most of the US.

The resulting isotropic 3D model systematically misfits Rayleigh and Love wave speeds between 10 and 20 sec period in some regions, overpredicting Rayleigh wave speeds and underpredicting Love wave speeds. We argue that this Rayleigh/Love discrepancy probably results from radial anisotropy in the middle and/or lower crust. Crustal radial anisotropy is required primarily within the Basin and Range and other extensional provinces, with $Vsh > Vsv$ by about $\sim$1% in these regions. A more exhaustive study of the Rayleigh/Love discrepancy using alternative model parameterizations, higher resolution data (e.g., from the USArray Transportable Array), and other kinds of data (e.g., receiver functions) is a natural extension of this work.

8. Acknowledgements

All of the data used in this research were downloaded either from the IRIS Data Management Center or the Canadian National Data Center (CNDC). This research was partially supported by a contract from the US Department of Energy, DE-FC52-2005NA26607, and two grants from the US National Science Foundation, EAR-0450082 and EAR-0711526. We are grateful for the support of Chuck Meertens throughout this project and the GEON project support for GDB (EAR-0408228).

References

Alsina, D., R. L. Woodward, and R. K. Snieder (1996), Shear wave velocity structure in North America from large-scale waveform inversions of surface waves, *J. Geophys. Res.*, *101*(B7), 15,969–15,986.

Barmin, M. P., M. H. Ritzwoller, and A. L. Levshin (2001), A fast and reliable method for surface wave tomography, *Pure Appl. Geophys.*, *158*(8), 1351–1375.

Bassin, C., G. Laske, and G. Masters (2000), The current limits of resolution for surface wave tomography in North America, *EOS Trans. AGU*, *81*, F897.

Bensen, G. D., M. H. Ritzwoller, M. P. Barmin, A. L. Levshin, F. Lin, M. P. Moschetti, N. M. Shapiro, and Y. Yang (2007a), Processing seismic ambient noise data to obtain reliable broad-band surface wave dispersion measurements, *Geophys. J. Int.*, *169*, 1239–1260.

Bensen, G. D., M. H. Ritzwoller, and N. M. Shapiro (2007b), Broad-band ambient noise surface wave tomography across the united states, *J. Geophys. Res.*, “accepted”.

Blackwell, D., J. Steele, and L. Carter (1990), Heat flow patterns of the North American continent: A discussion of the DNAG Geothermal Map of North America.

Christensen, N. I., and W. D. Mooney (1995), Seismic velocity structure and composition of the continental crust: A global view, *J. Geophys. Res.*, *100*(B6), 9761–9788.

Chulick, G. S., and W. D. Mooney (2002), Seismic structure of the crust and uppermost mantle of North America and adjacent oceanic basins: A synthesis, *Bull. Seis. Soc. Am.*, *92*(6), 2478–2492.

Crampin, S. (1970), The dispersion of surface waves in multilayered anisotropic media, *Geophys. J. Astr. Soc.*, *21*, 387–402.

Crampin, S., and S. Peacock (2005), A review of shear-wave splitting in the compliant crack-critical anisotropic Earth, *Wave Motion*, *41*(1), 59–77.

Crotwell, H. P., and T. J. Owens (2005), Automated receiver function processing, *Seis. Res. Lett.*, *76*(6), 702–709.

Dziewonski, A. M., and D. L. Anderson (1981), Preliminary reference Earth model, *Phys. Earth Plan. Int.*, *25*(4), 297–356.

Ekström, G., J. Tromp, and E. W. F. Larson (1997), Measurements and global models of surface wave propagation, *J. Geophys. Res.*, *102*(B4), 8137–8157.

Forsyth, D. W., and A. Li (2005), Array-analysis of Two-dimensional Variations in Surface Wave Phase Velocity and Azimuthal Anisotropy in the Presence of Multipathing Interference, *Seismic Earth: Array Analysis of Broadband Seismograms*, pp. 81–98.

Gao, W., S. P. Grand, W. S. Baldridge, D. Wilson, M. West, J. F. Ni, and R. Aster (2004), Upper mantle convection beneath the central Rio Grande Rift imaged by P and S wave tomography, *J. Geophys. Res.*, *109*(B03), 3305–3305.

Godey, S., R. K. Snieder, A. Villaseñor, and H. M. Benz (2003), Surface wave tomography of North America and the Caribbean using global and regional broad-band networks: phase velocity maps and limitations of ray theory, *Geophys. J. Int.*, *152*(3), 620–632.

Grand, S. P. (1994), Mantle shear structure beneath the Americas and surrounding oceans, *J. Geophys. Res.*, *99*(B6), 11,591–11,622.

Grand, S. P. (2002), Mantle shear-wave tomography and the fate of subducted slabs, *Philosophical Transactions: Mathematical, Physical and Engineering Sciences*, *360*(1800), 2475–2491.

Herrmann, R. B. (1987), Computer programs in seismology, *St. Louis University, St. Louis, Missouri.*

Jones, C. H., H. Kanamori, and S. W. . Roecker (1994), Missing roots and mantle "drips": Regional Pn and teleseismic arrival times in the southern Sierra Nevada and vicinity, California, *J. Geophys. Res.*, *99*(B3), 4567–4601.

Karlstrom, K. E., et al. (2002), CD-ROM working group. 2002. Structure and evolution of the lithosphere beneath the Rocky Mountains: initial results from the CD-ROM experiment, *GSA Today*, *12*(3), 4–10.

Keilis-Borok, V. I., and T. B. Yanovskaya (1967), Inverse problems in seismology (structural review), *Geophys. J. Astr. Soc.*, *13*, 223–234.

Kennett, B. L. N., E. R. Engdahl, and R. Buland (1995), Constraints on seismic velocities in the Earth from traveltimes, *Geophys. J. Int*, *122*(1), 108–124.

Laske, G., and G. Masters (1997), A global digital map of sediment thickness, *EOS Trans. AGU*, *78*, 483.

Lee, W. B., and S. C. Solomon (1978), Simultaneous inversion of surface wave phase velocity and attenuation: Love waves in western North America, *J. Geophys. Res.*, *83*(B7), 3389–3400.

Levshin, A., and L. Ratnikova (1984), Apparent anisotropy in inhomogeneous media, *J. Astron. Soc.*, *76*(1), 65–69.

Levshin, A. L., V. F. Pisarenko, and G. A. Pogrebinsky (1972), On a frequency-time analysis of oscillations, *Ann. Geophys.*, *28*(2), 211–218.

Li, A., D. W. Forsyth, and K. M. Fischer (2003), Shear velocity structure and azimuthal anisotropy beneath eastern North America from Rayleigh wave inversion, *J. Geophys.*

Res., *108*(10.1029).

Lin, F., M. P. Moschetti, and M. H. Ritzwoller (2007), Surface wave tomography of the western United States from ambient seismic noise: Rayleigh and Love wave phase velocity maps, *Geophys. J. Int.*, submitted.

Marone, F., and B. Romanowicz (2007), Non-linear crustal corrections in high-resolution regional waveform seismic tomography, *Geophys. J. Int.*, *170*(1), 460–467.

Marone, F., Y. Gung, and B. Romanowicz (2007), Three-dimensional radial anisotropic structure of the North American upper mantle from inversion of surface waveform data, *Geophys. J. Int.*, *171*(1), 206–222, doi:10.1111/j.1365-246X.2007.03465.x.

Masters, G., M. P. Barmine, and S. Kientz (2007), MINEOS user manual version 1.0, *Computational Infrastructure for Geodynamics*, http://www.geodynamics.org/cig/software/packages/seismo/mineos/ .

Montagner, J. P. (1991), Global upper mantle tomography of seismic velocities and anisotropies, *J. Geophys. Res.*, *96*(B12), 20,337–20,351.

Moschetti, M. P., M. H. Ritzwoller, and N. M. Shapiro (2007), Surface wave tomography of the western United States from ambient seismic noise: Rayleigh wave group velocity maps, *Geochem. Geophys. Geosys.*, *8*(Q08010), doi:10.1029/2007GC001655.

Mosegaard, K., and A. Tarantola (1995), Monte Carlo sampling of solutions to inverse problems, *J. Geophys. Res.*, *100*(B7), 12,431–12,448.

Nolet, G. (1990), Partitioned waveform inversion and two-dimensional structure under the network of autonomously recording seismographs, *J. Geophys. Res.*, *95*(B6), 8499–8512.

Ozalaybey, S., M. K. Savage, A. F. Sheehan, J. N. Louie, and J. N. Brune (1997), Shear-wave velocity structure in the northern Basin and Range province from the combined analysis of receiver functions and surface waves, *Bull. Seis. Soc. Am.*, *87*(1), 183–199.

Ramachandran, K., S. E. Dosso, G. D. Spence, R. D. Hyndman, and T. M. Brocher (2005), Forearc structure beneath southwestern British Columbia: A three-dimensional tomographic velocity model, *J. Geophys. Res.*, *110*(B2), 2303(17), doi: 10.1029/2004JB003258.

Ritzwoller, M. H., and A. L. Levshin (1998), Eurasian surface wave tomography - group velocities, *J. Geophys. Res.*, *103*(B3), 4839–4878.

Ritzwoller, M. H., N. M. Shapiro, M. P. Barmin, and A. L. Levshin (2002), Global surface wave diffraction tomography, *J. Geophys. Res.*, *107*(B12), 2335–2347, doi: 10.1029/2002JB001777.

Saito, M. (1988), DISPER80: A subroutine package for the calculation of seismic normal-mode solutions, in *Seismological algorithms: Computational methods and computer programs*, edited by D. Doornbos, Academic Press, San Diego, Calif.

Sambridge, M., and K. Mosegaard (2002), Monte Carlo methods in geophysical inverse problems, *Rev. Geophys*, *40*(3), 3–32.

Shapiro, N. M., and M. H. Ritzwoller (2002), Monte-Carlo inversion for a global shear-velocity model of the crust and upper mantle, *Geophys. J. Int.*, *151*(1), 88–105.

Shapiro, N. M., M. H. Ritzwoller, P. H. Molnar, and V. Levin (2004), Thinning and flow of Tibetan crust constrained by seismic anisotropy, *Science*, *305*(5681), 233–236.

Snelson, C. M., T. J. Henstock, G. R. Keller, K. C. Miller, and A. Levander (1998), Crustal and uppermost mantle structure along the Deep Probe seismic profile, *Rocky Mountain Geology*, *33*(2), 181–198.

Snieder, R. K. (1988), Large-scale waveform inversions of surface waves for lateral heterogeneity 1. Theory and numerical examples, *J. Geophys. Res.*, *93*(B10), 12,055–12,065.

Tanimoto, T., and D. L. Anderson (1984), Mapping convection in the mantle, *Geophys. Res. Lett.*, *11*(4), 287–290.

Tarantola, A., and B. Valette (1982), Generalized nonlinear inverse problems solved using the least squares criterion, *Rev. Geophys. Space Phys*, *20*(2), 219–232.

Thurber, C., H. Zhang, F. Waldhauser, J. Hardebeck, A. Michael, and D. Eberhart-Phillips (2006), Three-dimensional compressional wavespeed model, earthquake relocations, and focal mechanisms for the Parkfield, California, region, *Bull. Seis. Soc. of Am.*, *96*(4 B), 38–49.

Trampert, J., and J. H. Woodhouse (1996), High resolution global phase velocity distributions, *Geophys. Res. Lett.*, *23*(1), 21–24.

van der Lee, S. (2002), High-resolution estimates of lithospheric thickness from Missouri to Massachusetts, USA, *Earth Plan. Sci. Lett.*, *203*(1), 15–23.

van der Lee, S., and A. Frederiksen (2005), Surface wave tomography applied to the North American upper mantle, *Geophysical monograph*, *157*, 67–80.

van der Lee, S., and G. Nolet (1997), Upper mantle S velocity structure of North America, *J. Geophys. Res.*, *102*(B10), 22,815–22,838.

Villaseñor, A., M. H. Ritzwoller, A. L. Levshin, M. P. Barmin, E. R. Engdahl, W. Spakman, and J. Trampert (2001), Shear velocity structure of central Eurasia from inversion of surface wave velocities, *Phys. Earth Planet. Inter*, *123*(1), 169–184.

Weeraratne, D. S., D. W. Forsyth, K. M. Fischer, and A. A. Nyblade (2003), Evidence for an upper mantle plume beneath the Tanzanian craton from Rayleigh wave tomography, *J. Geophys. Res.*, *108*(B9), 2427–2446.

Wernicke, B. P., G. J. Axen, and J. K. Snow (1988), Basin and Range extensional tectonics at the latitude of Las Vegas, Nevada, *Bull. Geol. Soc. Am.*, *100*(11), 1738–1757.

Wilson, C. K., C. H. Jones, and H. J. Gilbert (2003), Single-chamber silicic magma system inferred from shear wave discontinuities of the crust and uppermost mantle, coso geothermal area, California, *J. Geophys. Res*, *108*, 1–16.

Yang, Y. and D.W. Forsyth (2006), Rayleigh wave phase velocities, small-scale convection, and azimuthal anisotropy beneath Southern California, *J. Geophys. Res*, *111*, B07306, doi:10.1029/2005JB004180.

Yang, Y., M. H. Ritzwoller, A. L. Levshin, and N. M. Shapiro (2007a), Ambient noise Rayleigh wave tomography across Europe, *Geophys. J. Int.*, *168*(1), 259–274.

Yang, Y., A. Li, and M.H. Ritzwoller (2007b), Crustal and uppermost mantle structure in southern Africa revealed from ambient noise and teleseismic tomography, *Geophys. J. Int.*, in press.

Yao, H., R. D. van der Hilst, and M. V. de Hoop (2006), Surface-wave array tomography in SE Tibet from ambient seismic noise and two-station analysis-I. Phase velocity maps, *Geophys. J. Int.*, *166*(2), 732–744.

Yuan, H., and K. Dueker (2005), Upper mantle tomographic Vp and Vs images of the Rocky Mmountains in Wyoming, Colorado and New Mexico: Evidence for a thick heterogeneous chemical lithosphere, *Geophysical Monograph*, *154*, 329–345.

Table 1. χ^2 misfit for Rayleigh and Love waves averaged from 8 to 20 sec period across Nevada. Column 1 lists the method of crustal model parameterization, where "Monotonic Isotropic" denotes 3 crustal layers of monotonically increasing isotropic velocity with depth, "Nonmonotonic Isotropic" is also isotropic but with the monotonicity constraint removed for 4 crustal layers, and "Radial Anisotropy" is where radial anisotropy is allowed in the middle of the 3 crustal layers. Columns 2, 3, and 4 indicate χ^2 values for Love wave phase speed, Rayleigh wave phase speed, and the average of the two. The final column lists the variance reduction over the monotonic isotropic parameterization.

Param. type	χ^2-Love	χ^2-Rayleigh	χ^2-avg.	Variance Reduction
Monotonic Isotropic	2.21	1.42	1.81	
Nonmonotonic Isotropic	1.45	1.63	1.54	15.2%
Radial Anisotropy	1.05	1.07	1.06	41.6%

Figure 1. Map of the study area showing stations used in the experiment as black triangles. Grey circles, squares, and a star are the locations for the examples in Figures 6, 7, 8, and 19.

Figure 2. Regions and geographic features. The black contour surrounds the area with lateral resolution better than 500 km for the 16 s Rayleigh wave phase velocity. Tectonic provinces are outlined in red and are labeled (bounded by rectangles) for reference. Features (from east to west) are as follows: Appalachian Highlands(ApH), Ouachita-Ozark Highlands (OH), Central Lowlands (CL), Great Plains (GP), Rocky Mountain Region (RM), Colorado Plateau (CP), Basin and Range (B&R), Columbia Plateau (CP), Sierra Nevada Mountains (SN), and Great Valley (GV). Other features are labeled (bounded by ellipses) as follows: Appalachian Basin (ApB), Michigan Basin (MB), Mississippi Embayment (ME), Mid-continental Rift (MCR), Anadarko Basin (AB), Williston Basin (WB), Rio Grande Rift (RGR), Green River Basin (GRB), Gulf of California (GC), and Pacific Northwest (PNW).

Figure 3. Sensitivity kernels for Rayleigh (labeled RC) and Love (labeled LC) wave phase speeds at a selection of periods.

Figure 4. Average measurement uncertainty for the Rayleigh wave group and phase speed and the Love wave phase speed maps. These are the average values within which we attempt to fit the data.

Figure 5. An illustration of the parameterization of the models used to create dispersion curves for (a) the linearized inversion and (b) the Monte-Carlo inversion. Fifteen layers are used in the mantle for the linearized inversion while five B-splines are used in the mantle for the Monte-Carlo inversion.

Figure 6. Example of the best fitting model and dispersion curves from the linearized inversion for a point in Illinois. Rayleigh and Love wave phase speed measurements and uncertainties are represented with error bars in (a). The input model in (b) and related dispersion curves in (a) are shown as grey dashed lines. The estimated models and dispersion curves are thin black lines in (b) and (a). The latitude, longitude and approximate location is listed in (b) and labeled as a grey circle in Figure 1. Velocity values at the center of each mantle layer are plotted.

Figure 7. Same as Figure 6 but for points in California and Montana, shown as grey circles in Figure 1. The χ^2 values indicated in (a) and (c) are toward the larger end in this study.

Figure 8. Examples of the input and output dispersion curves (error bars and grey lines, respectively, in (b), (d), and (f)) and the resulting ensemble of Monte-Carlo models ((a), (c), and (e)). The "favored model" is drawn in red. Locations of the examples presented here are shown as grey squares in Figure 1.

Figure 9. Rayleigh and Love wave phase velocity χ^2 misfit values for the best fitting isotropic model at each point as determined through linearized inversion.

Figure 10. Representation of the short-period discrepancy between Rayleigh and Love waves from the isotropic "favored models" that emerge from the Monte Carlo inversion. The difference of the model predicted and measured wave speed is divided by the data error at each point for each period. The results presented here are the average of values from 8 - 20 s period. Greens/oranges indicate that the model is too fast and blues that the model is too slow.

Figure 11. A selection of horizontal V_s depth sections through the isotropic "favored model" from Monte-Carlo inversion. Panels (c) and (d) show the model at 4 km above and below the recovered Moho, respectively.

Figure 12. The crustal thickness of the "favored model" from the Monte-Carlo inversion. Crustal thickness is required to be within 5 km of the values of *Bassin et al.* [2000].

Figure 13. A selection of V_s vertical cross sections through the "favored model" from Monte-Carlo inversion. The locations of the cross-sections are indicated in (a) and the horizontal scale of all the cross-sections is the same. The recovered Moho is plotted in all cross-sections as a black line. Different color scales are used in the crust and mantle, as shown at bottom.

Figure 14. (a) The average standard deviation of the ensemble of models from the Monte Carlo inversion is plotted versus depth as the solid line. The dashed line is the mean of the absolute value of the velocity anomalies at each depth taken across the entire study region. (b) The standard deviation of the dispersion curves predicted by the ensemble of models averaged across all geographic points.

Figure 15. Horizontal slices showing the estimated standard deviation of the ensemble of V_s models derived from the Monte-Carlo inversion at the depths presented in Figure 11. Panels (c) and (d) are results at 4 km above and below the Moho, respectively.

Figure 16. Histograms of velocity values taken from the 0.5° grid east and west of the approximate location of the boundary of the crustal dichotomy in the lower crust and at 80 km depth across the profile at 40°N. The values are from the "favored model" and the boundary is defined at 3.75 and 4.55 km/s in the lower crust and mantle, respectively.

Figure 17. The location and uncertainty in the east-west shear velocity dichotomy for the lower crust (a) and the uppermost mantle (b). Contours of velocity are plotted for the 20th (grey) and 80th (black) percentile models at 3.75 km/s for the lower crust and 4.55 at 80 km in the mantle taken from the ensemble of accepted models determined by Monte Carlo inversion. The red contour marks the approximate location of the Rocky Mountain Front.

Figure 18. A comparison of the "favored model" from the Monte Carlo inversion with the global V_s model of *Shapiro and Ritzwoller* [2002], shown here in (a) at 40°N (Profile B-B' in Figure 13a), where the velocity scales from Figure 13 are used. (b) The model of *Shapiro and Ritzwoller* [2002] minus and our favored model. Reds indicated that the global model is fast and blues that it is slow relative to our model. The Moho contour from (a) is overplotted in (b).

Figure 19. An example of the improvement in fit afforded by allowing radial anisotropy or breaking the monotonicity constraint (allowing a low velocity zone, LVZ) in the crust. The dispersion curves for the monotonic isotropic, radial anisotropic, and LVZ model are labeled in (a) and the corresponding models are shown in (b). Radial anisotropy is allowed only in the middle crust.

Figure 20. (a) The best fitting middle crustal radial anisotropy model for the US where, for example, a value of 5% signifies $Vsh/Vsv = 1.05$. (b) The least anisotropic model from the ensemble of acceptable models that emerge from the Monte-Carlo inversion.

50
40
30
20
230
240
250
260
270
280
290

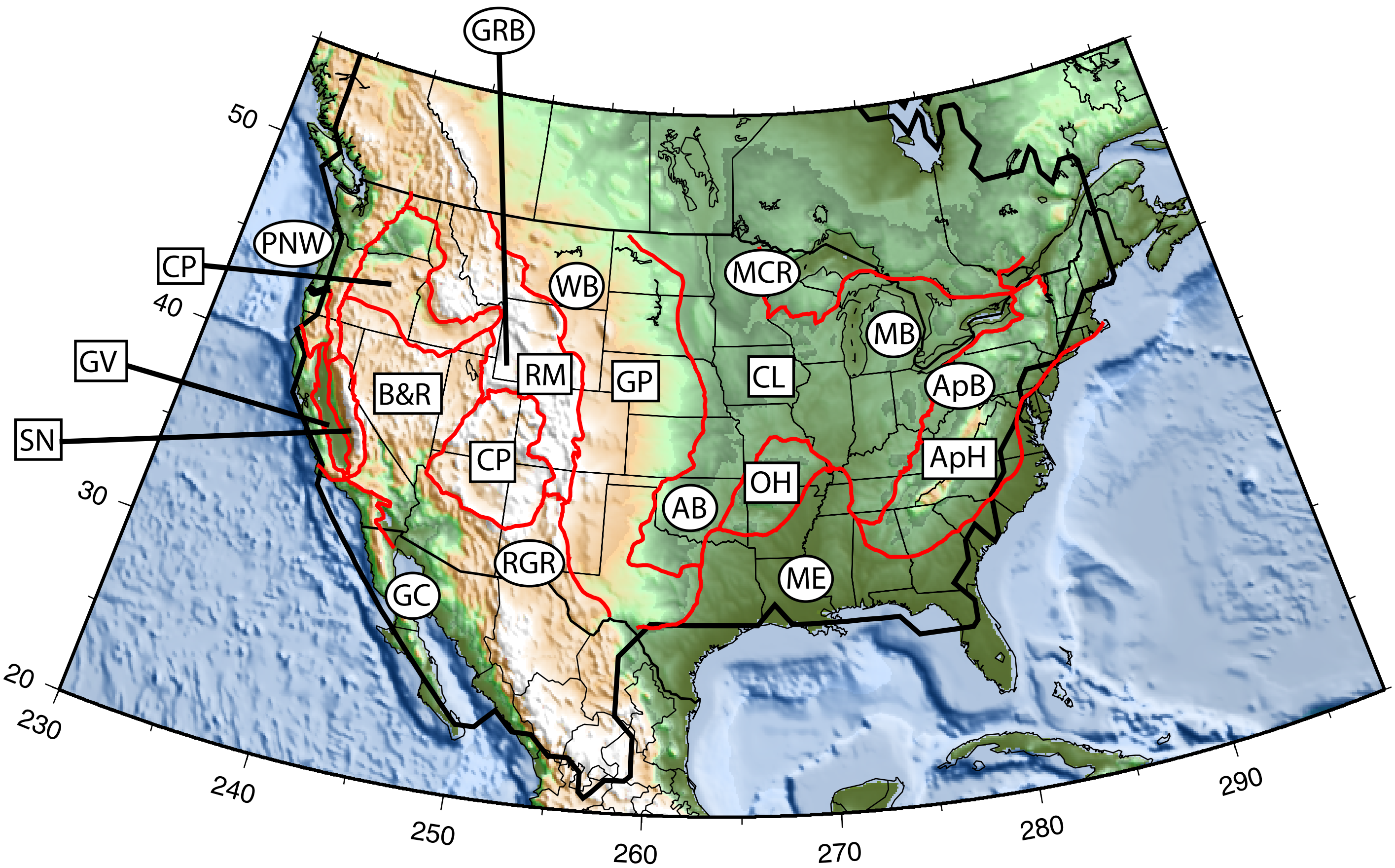

GRB
50
PNW
CP
WB
MCR
40
MB
GV
RM
GP
CL
B&R
ApB
SN
CP
ApH
OH
30
AB
RGR
ME
GC
20
230
240
250
260
270
280
290

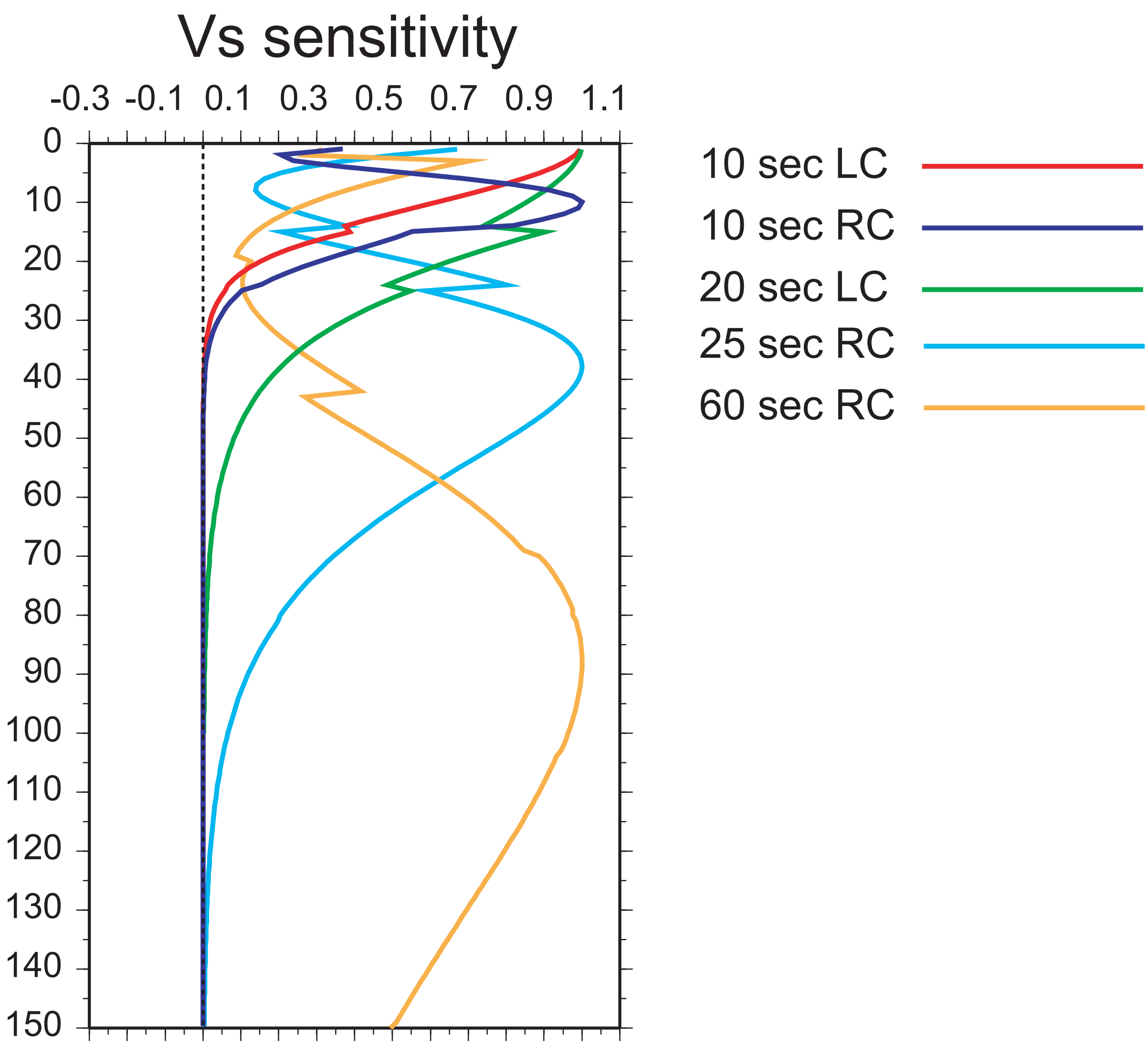

Vs sensitivity
-0.3
-0.1
0.1
0.3
0.5
0.7
0.9
1.1
0
10
20
30
40
50
60
70
80
90
100
110
120
130
140
150
10 sec LC
10 sec RC
20 sec LC
25 sec RC
60 sec RC

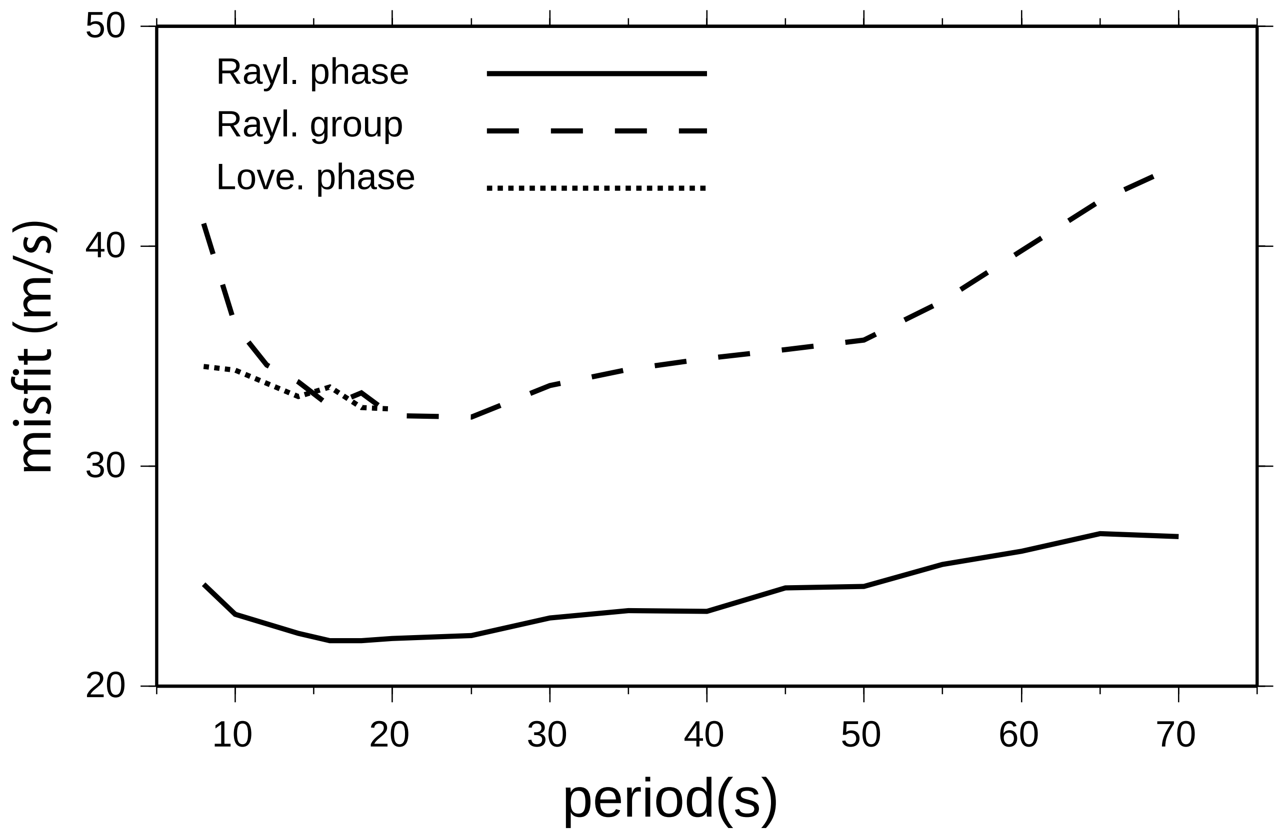
Rayl. phase
Rayl. group
Love. phase
misfit (m/s)
50
40
30
20
10
20
30
40
50
60
70
period(s)

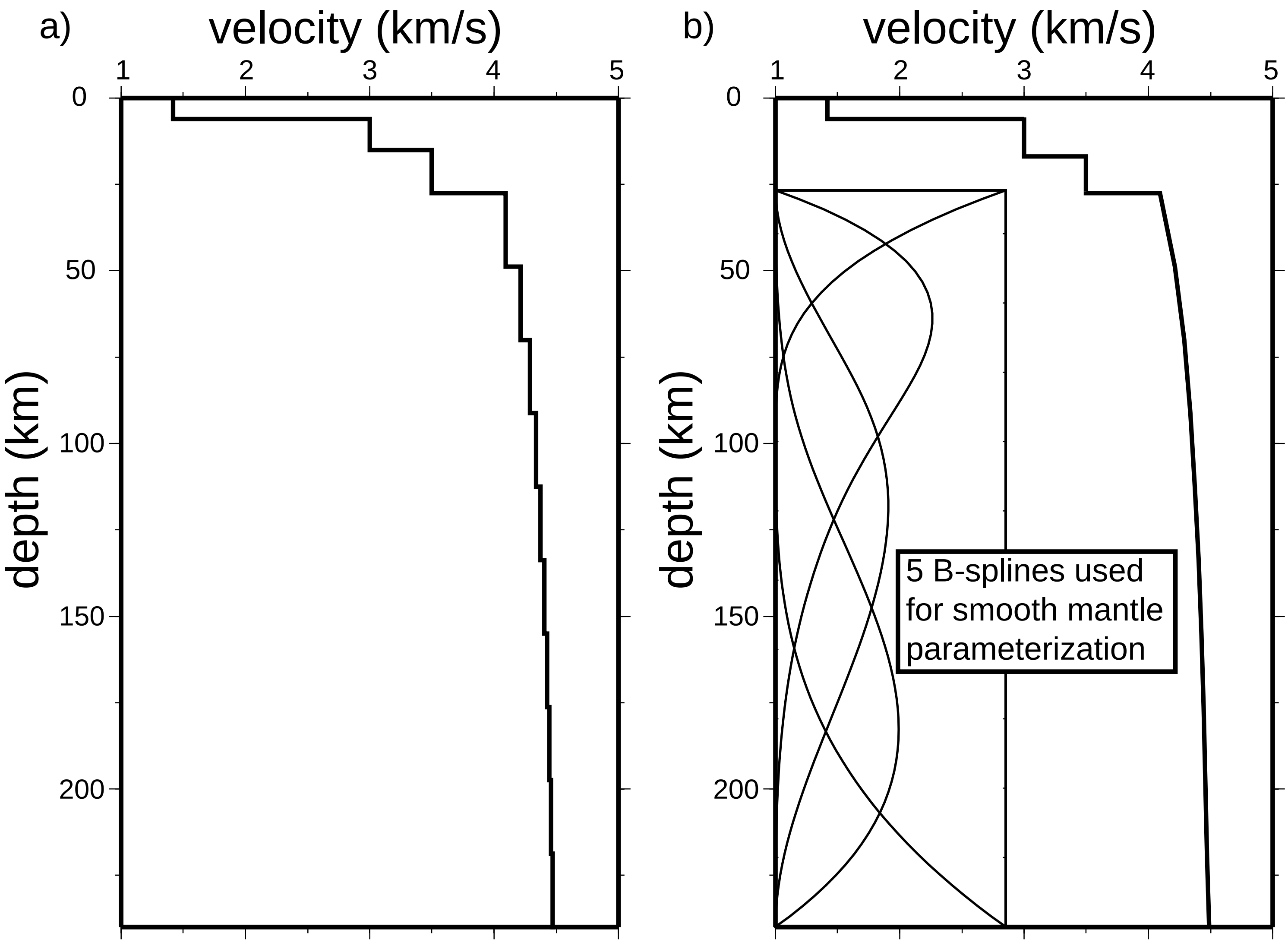
a)
velocity (km/s)
1
2
3
4
5
0
50
100
150
200
depth (km)
b)
velocity (km/s)
1
2
3
4
5
0
50
100
150
200
depth (km)
5 B-splines used
for smooth mantle
parameterization

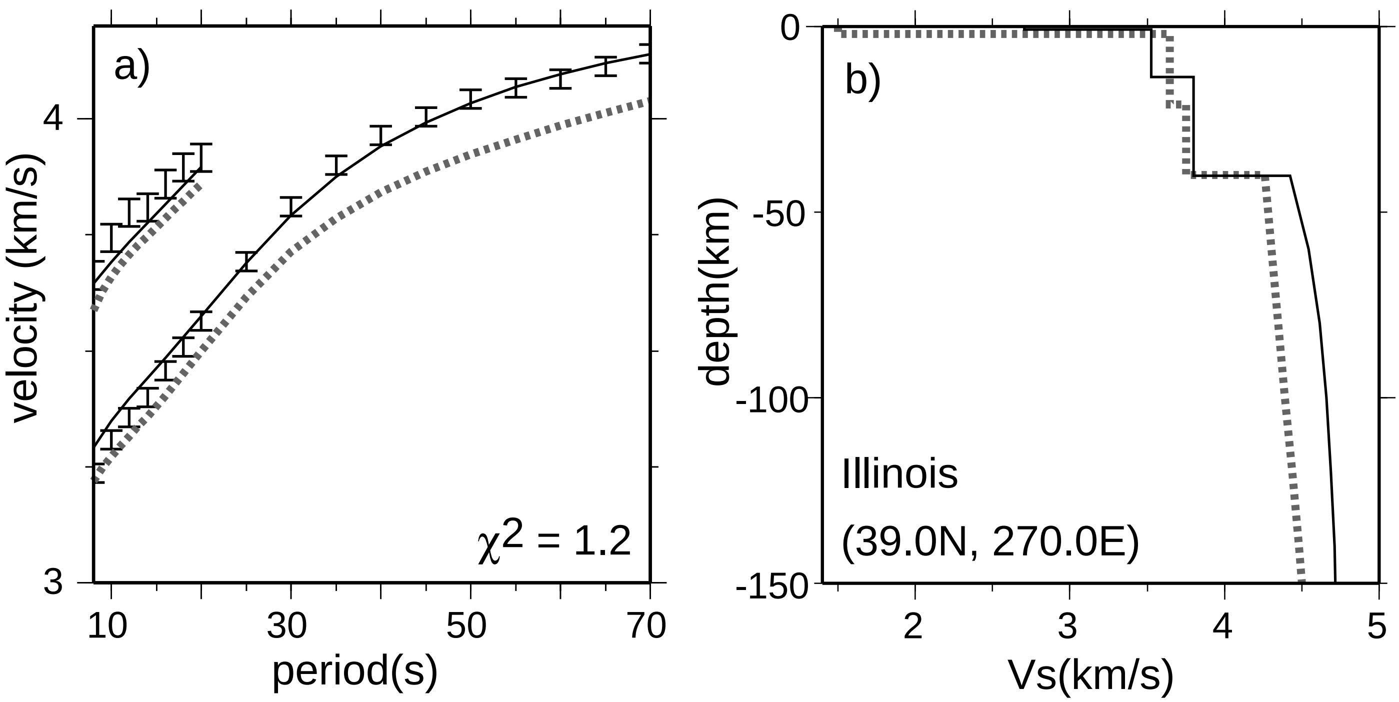
a)
velocity (km/s)
4
3
10
30
50
70
period(s)
χ^2 = 1.2
b)
0
-50
-100
-150
depth(km)
2
3
4
5
Vs(km/s)
Illinois
(39.0N, 270.0E)

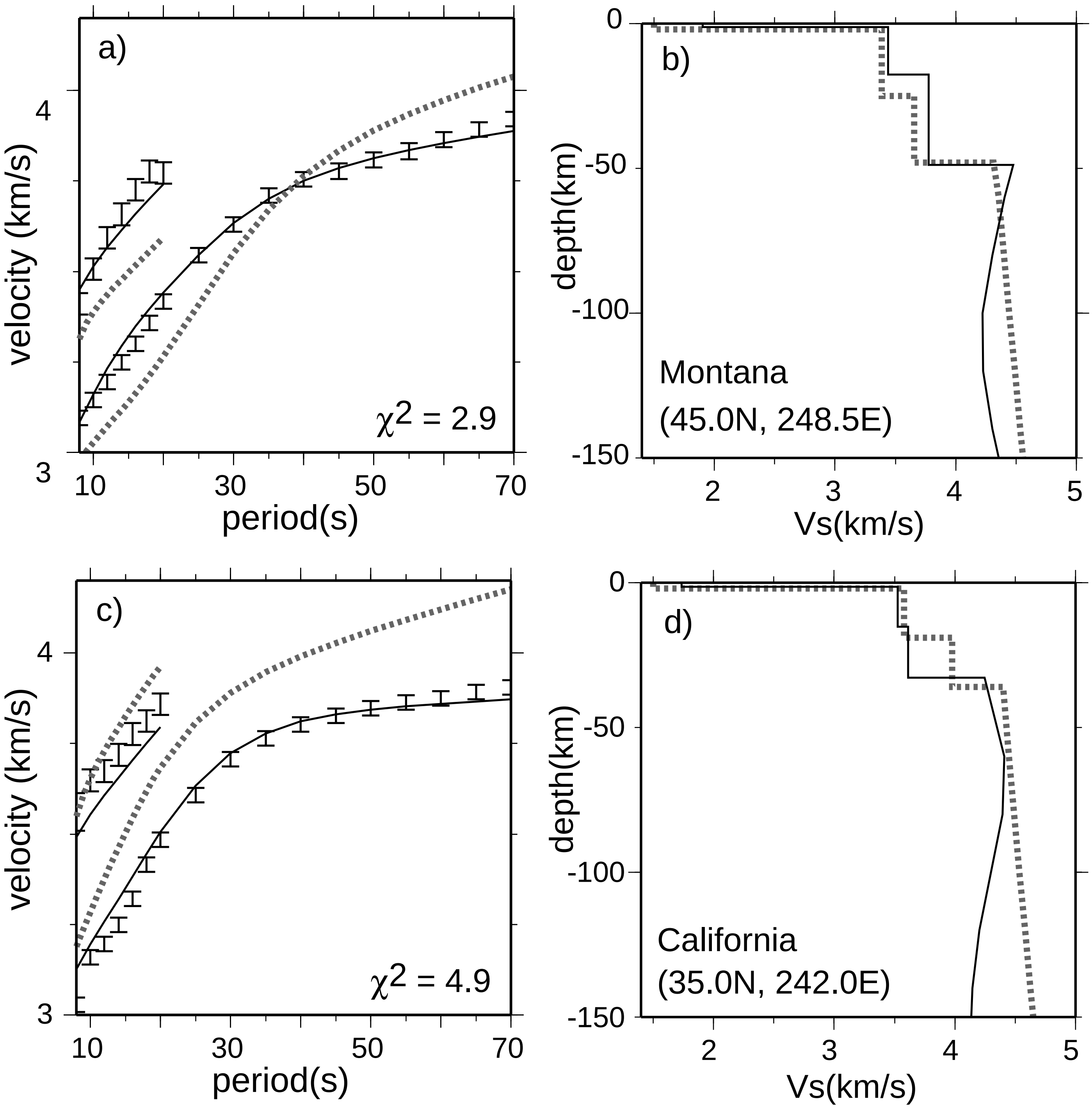
a)
velocity (km/s)
period(s)
χ2 = 2.9
b)
depth(km)
Vs(km/s)
Montana
(45.0N, 248.5E)
c)
velocity (km/s)
period(s)
χ2 = 4.9
d)
depth(km)
Vs(km/s)
California
(35.0N, 242.0E)

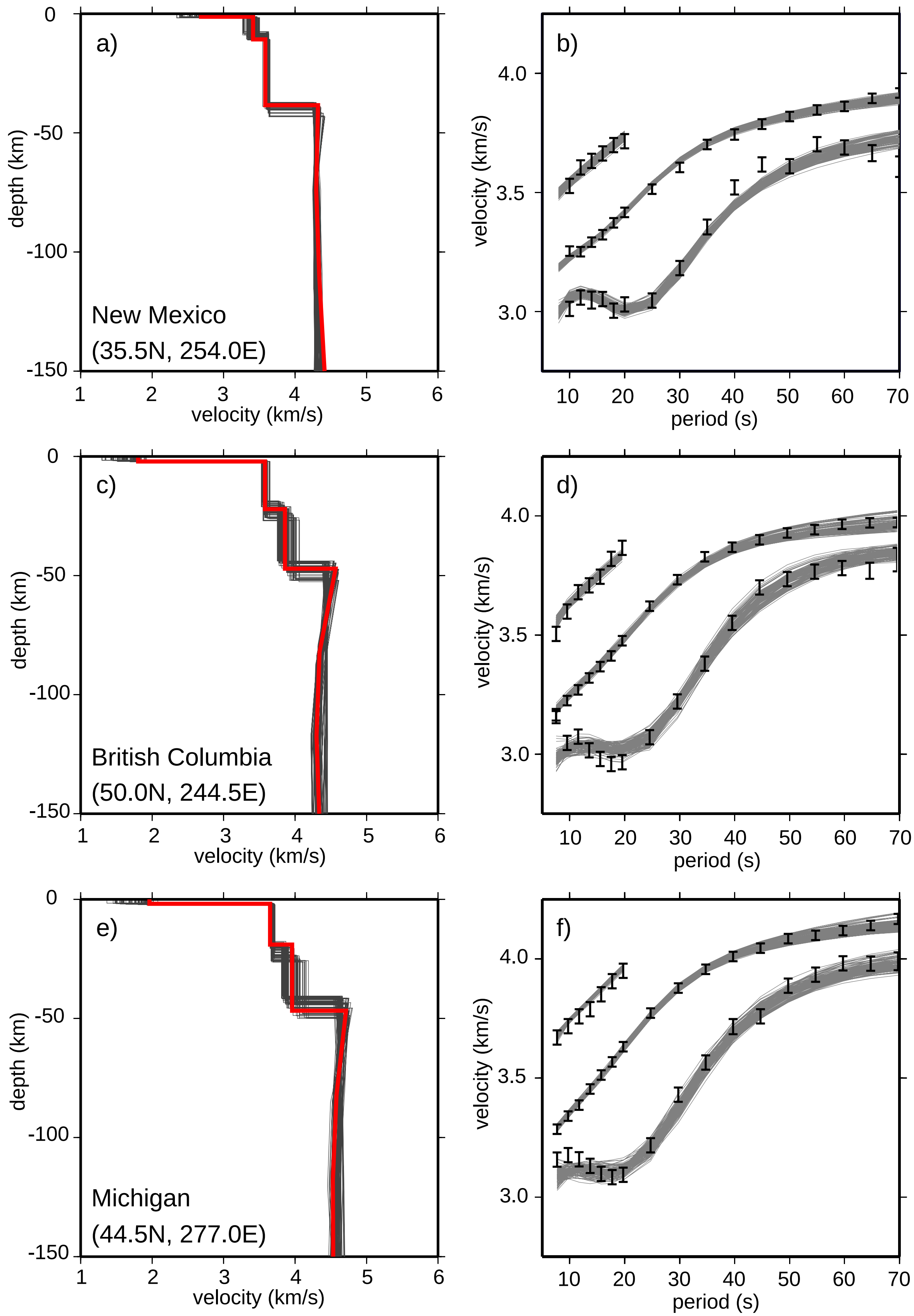
a)
New Mexico
(35.5N, 254.0E)
depth (km)
velocity (km/s)
b)
velocity (km/s)
period (s)
c)
British Columbia
(50.0N, 244.5E)
depth (km)
velocity (km/s)
d)
velocity (km/s)
period (s)
e)
Michigan
(44.5N, 277.0E)
depth (km)
velocity (km/s)
f)
velocity (km/s)
period (s)

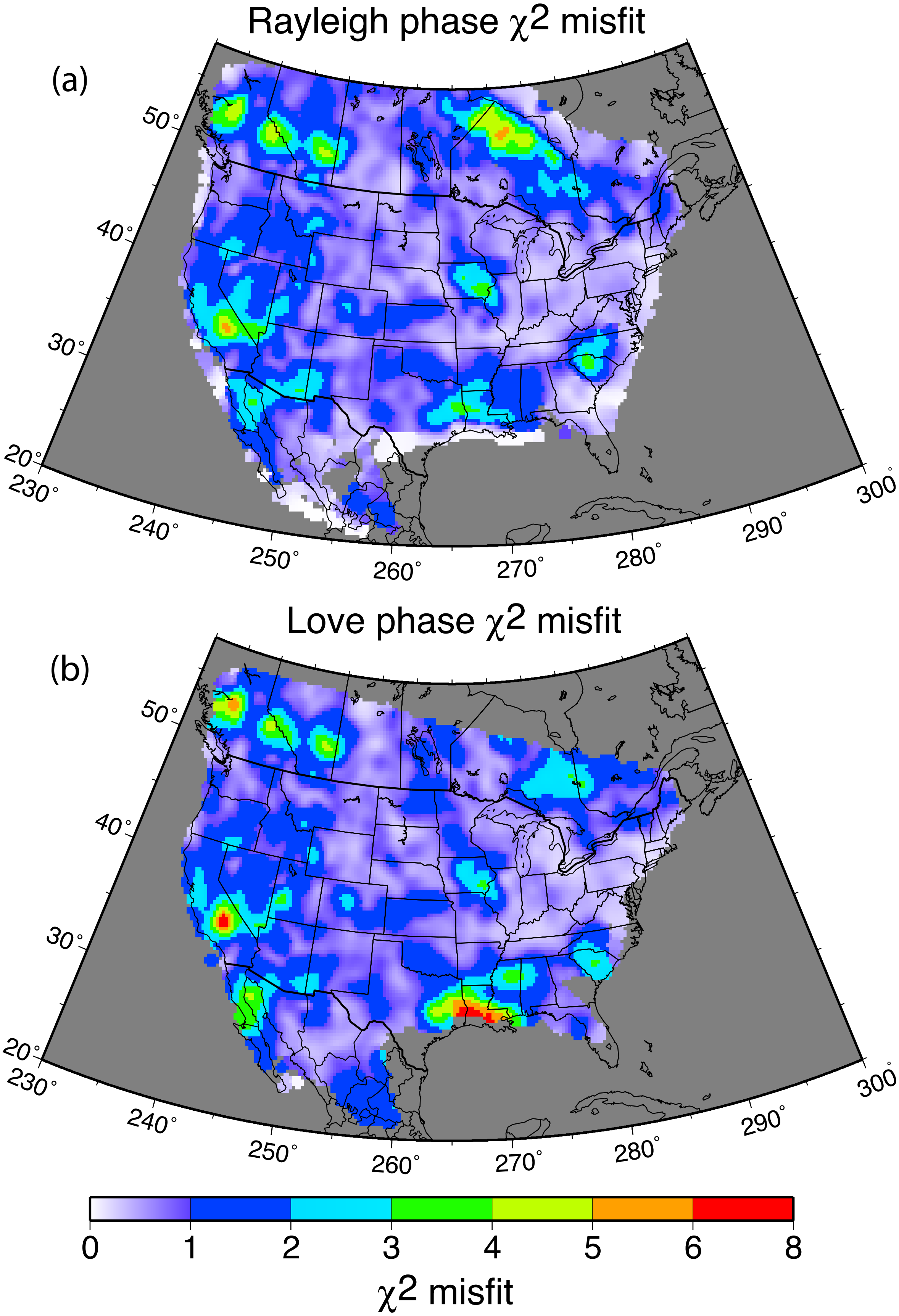

Rayleigh phase χ2 misfit
(a)
50°
40°
30°
20°
230°
240°
250°
260°
270°
280°
290°
300°
Love phase χ2 misfit
(b)
50°
40°
30°
20°
230°
240°
250°
260°
270°
280°
290°
300°
0
1
2
3
4
5
6
8
χ2 misfit

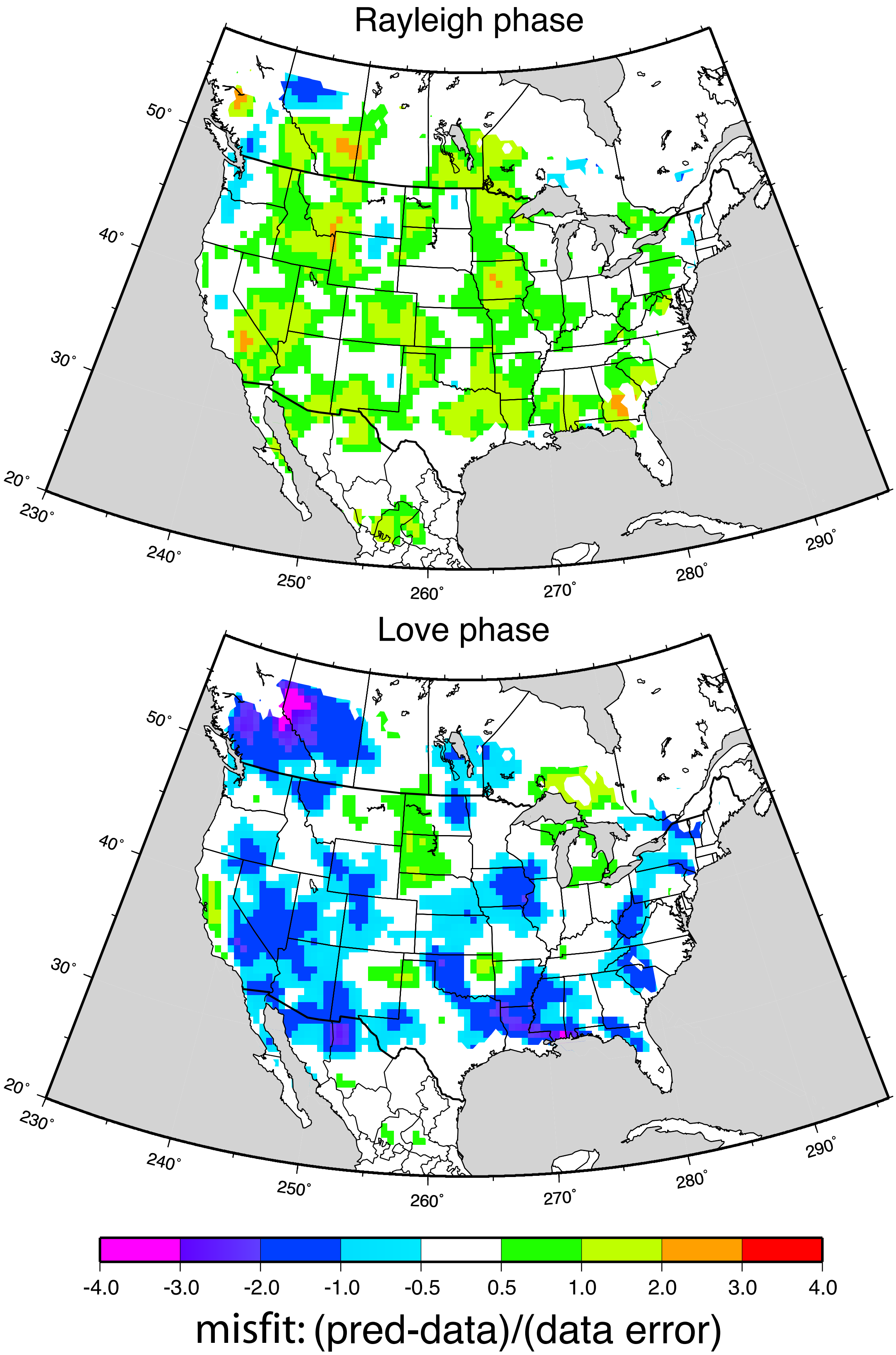
Rayleigh phase
50°
40°
30°
20°
230°
240°
250°
260°
270°
280°
290°
Love phase
50°
40°
30°
20°
230°
240°
250°
260°
270°
280°
290°
-4.0
-3.0
-2.0
-1.0
-0.5
0.5
1.0
2.0
3.0
4.0
misfit: (pred-data)/(data error)

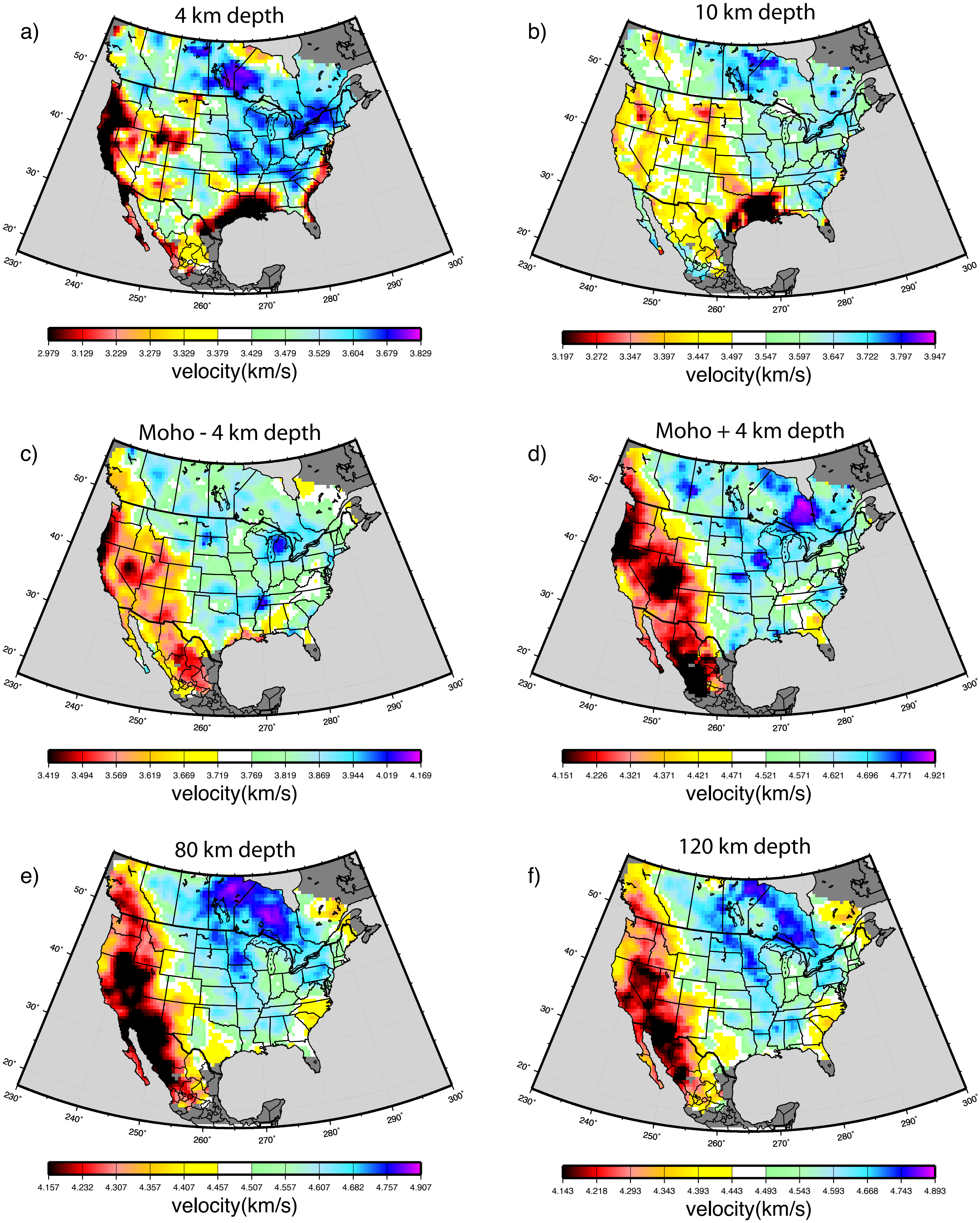

a)
4 km depth
2.979 3.129 3.229 3.279 3.329 3.379 3.429 3.479 3.529 3.604 3.679 3.829
velocity(km/s)
b)
10 km depth
3.197 3.272 3.347 3.397 3.447 3.497 3.547 3.597 3.647 3.722 3.797 3.947
velocity(km/s)
c)
Moho - 4 km depth
3.419 3.494 3.569 3.619 3.669 3.719 3.769 3.819 3.869 3.944 4.019 4.169
velocity(km/s)
d)
Moho + 4 km depth
4.151 4.226 4.321 4.371 4.421 4.471 4.521 4.571 4.621 4.696 4.771 4.921
velocity(km/s)
e)
80 km depth
4.157 4.232 4.307 4.357 4.407 4.457 4.507 4.557 4.607 4.682 4.757 4.907
velocity(km/s)
f)
120 km depth
4.143 4.218 4.293 4.343 4.393 4.443 4.493 4.543 4.593 4.668 4.743 4.893
velocity(km/s)

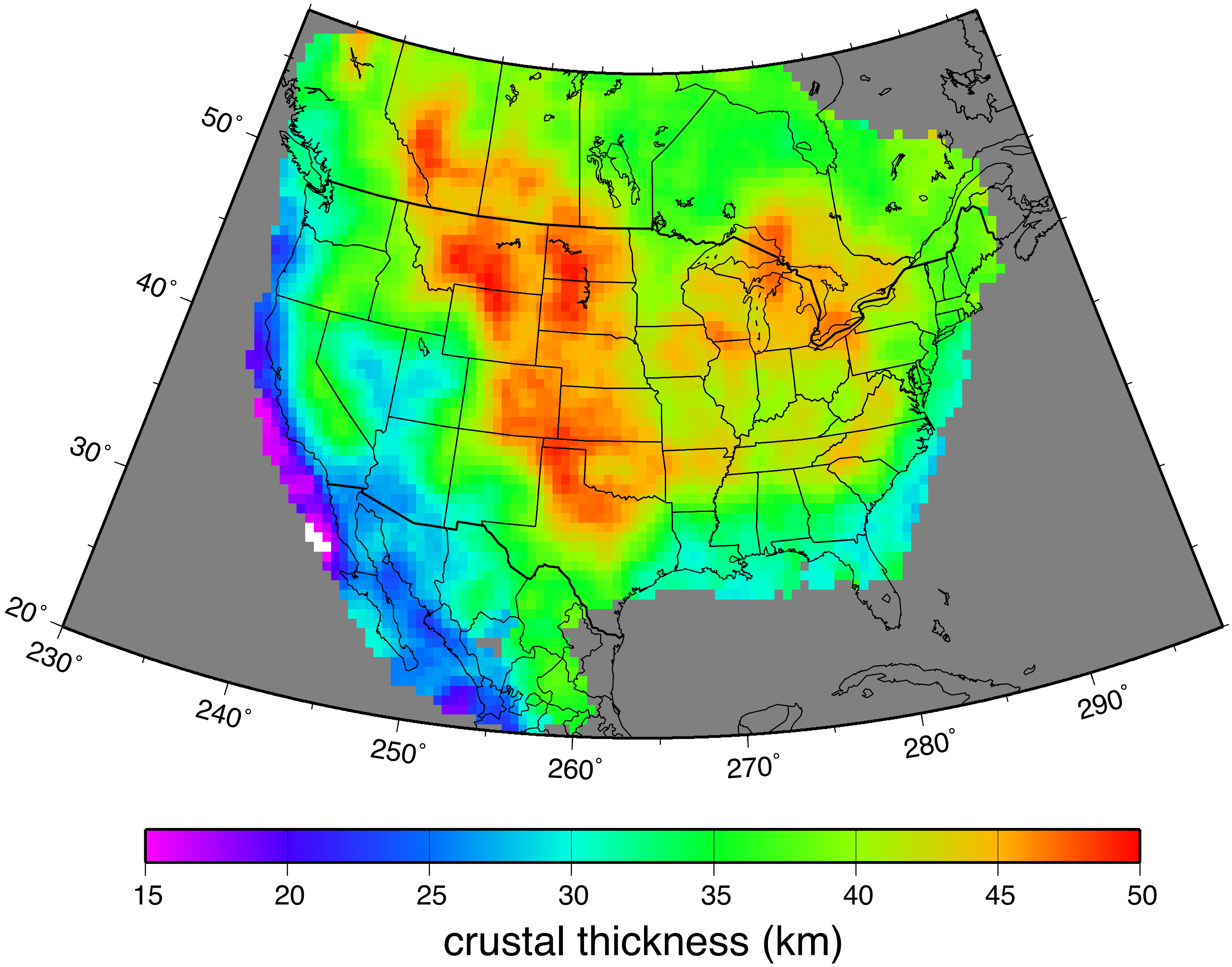
50°
40°
30°
20°
230°
240°
250°
260°
270°
280°
290°
15
20
25
30
35
40
45
50
crustal thickness (km)

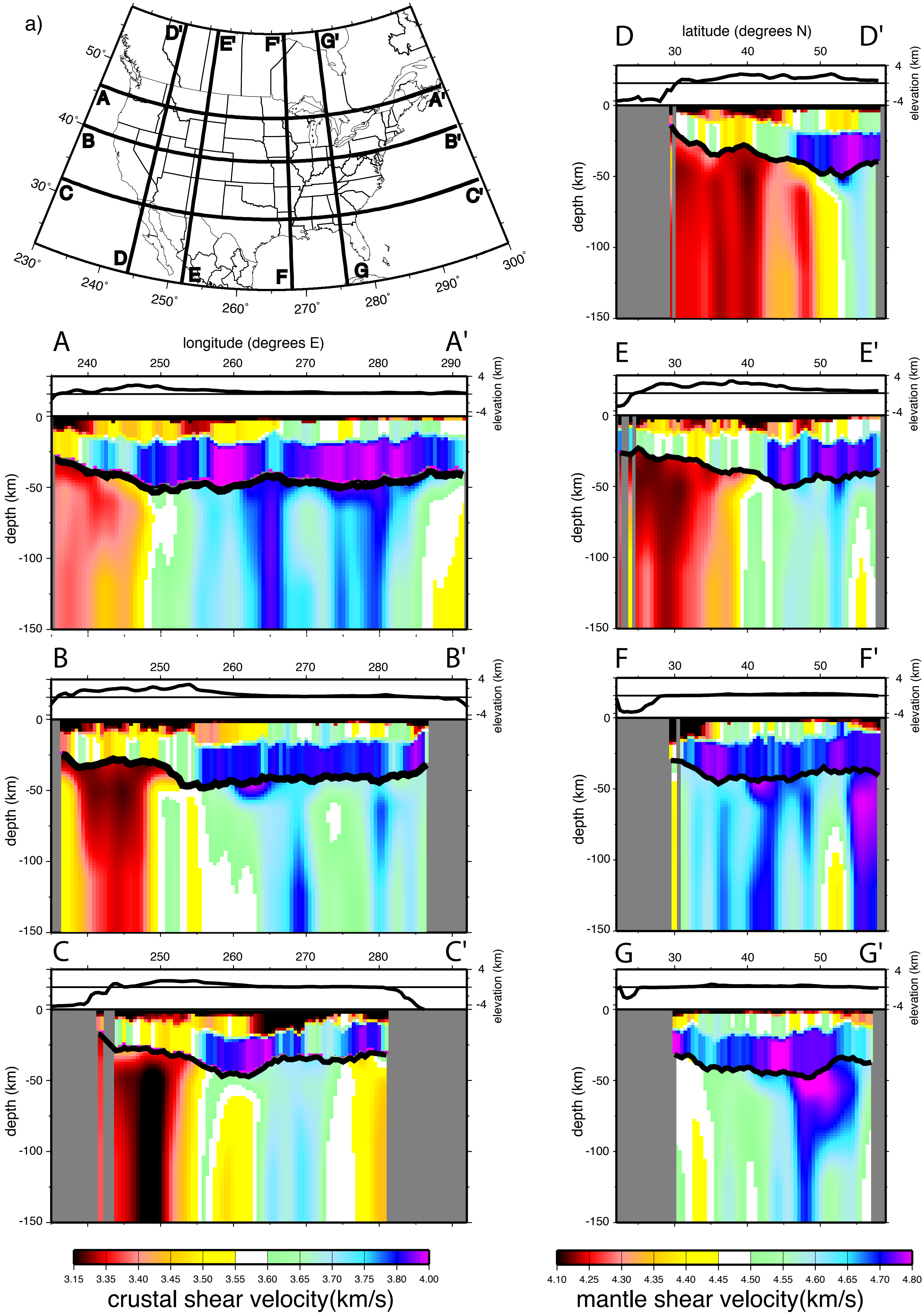

a)
A
A'
B
B'
C
C'
D
D'
E
E'
F
F'
G
G'
longitude (degrees E)
latitude (degrees N)
depth (km)
elevation (km)
crustal shear velocity(km/s)
mantle shear velocity(km/s)

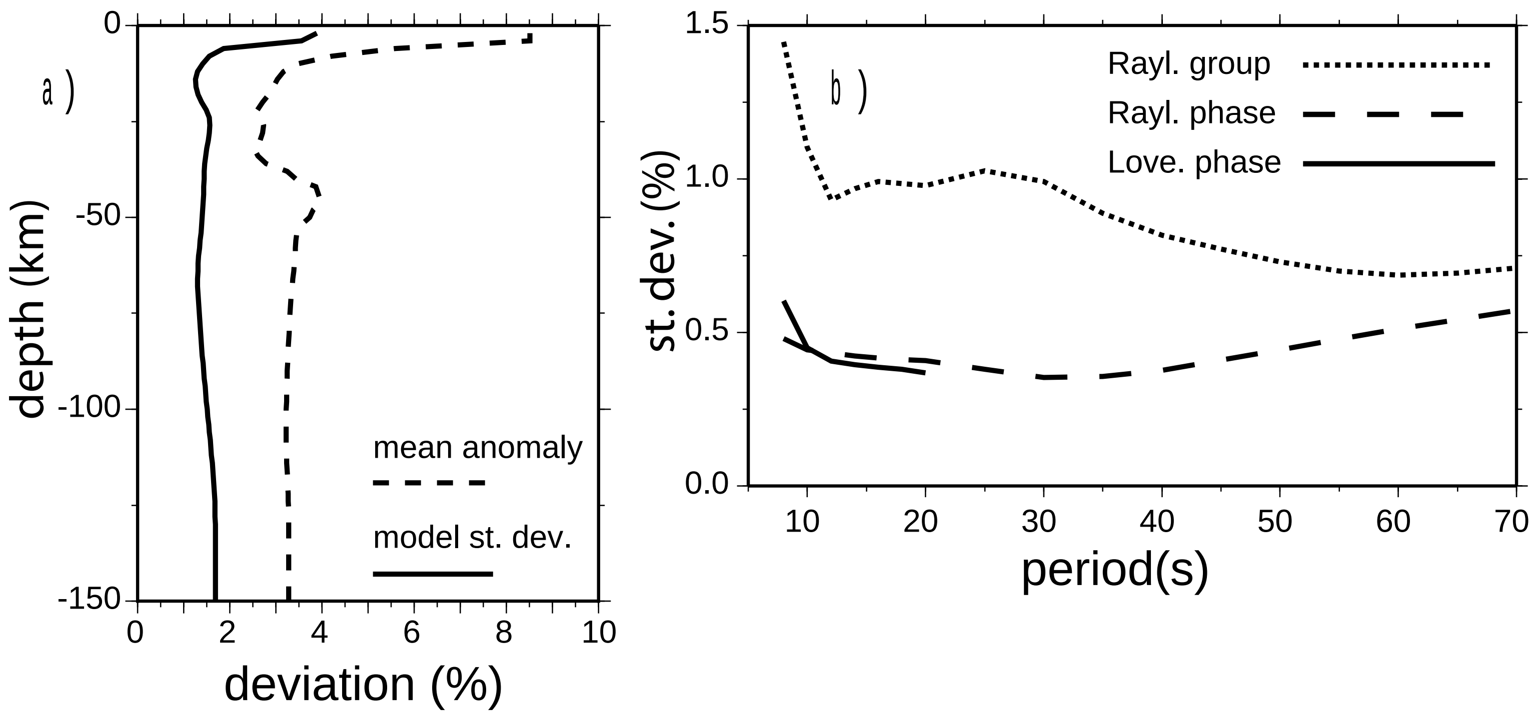

a)
0
-50
-100
-150
depth (km)
0
2
4
6
8
10
deviation (%)
mean anomaly
model st. dev.
b)
1.5
1.0
0.5
0.0
st. dev. (%)
10
20
30
40
50
60
70
period(s)
Rayl. group
Rayl. phase
Love. phase

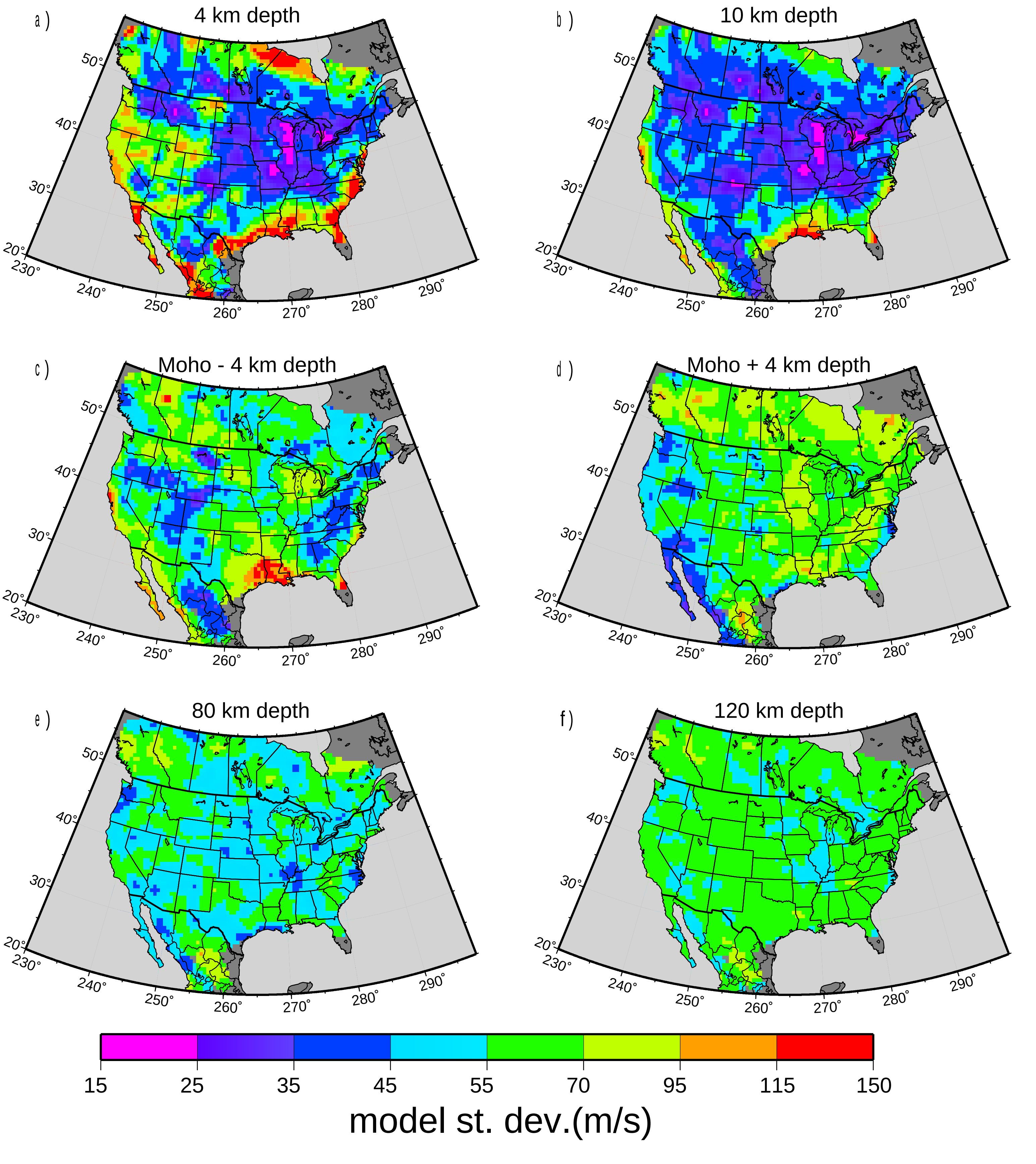
a)
4 km depth
b)
10 km depth
c)
Moho - 4 km depth
d)
Moho + 4 km depth
e)
80 km depth
f)
120 km depth
50°
40°
30°
20°
230°
240°
250°
260°
270°
280°
290°
15
25
35
45
55
70
95
115
150
model st. dev.(m/s)

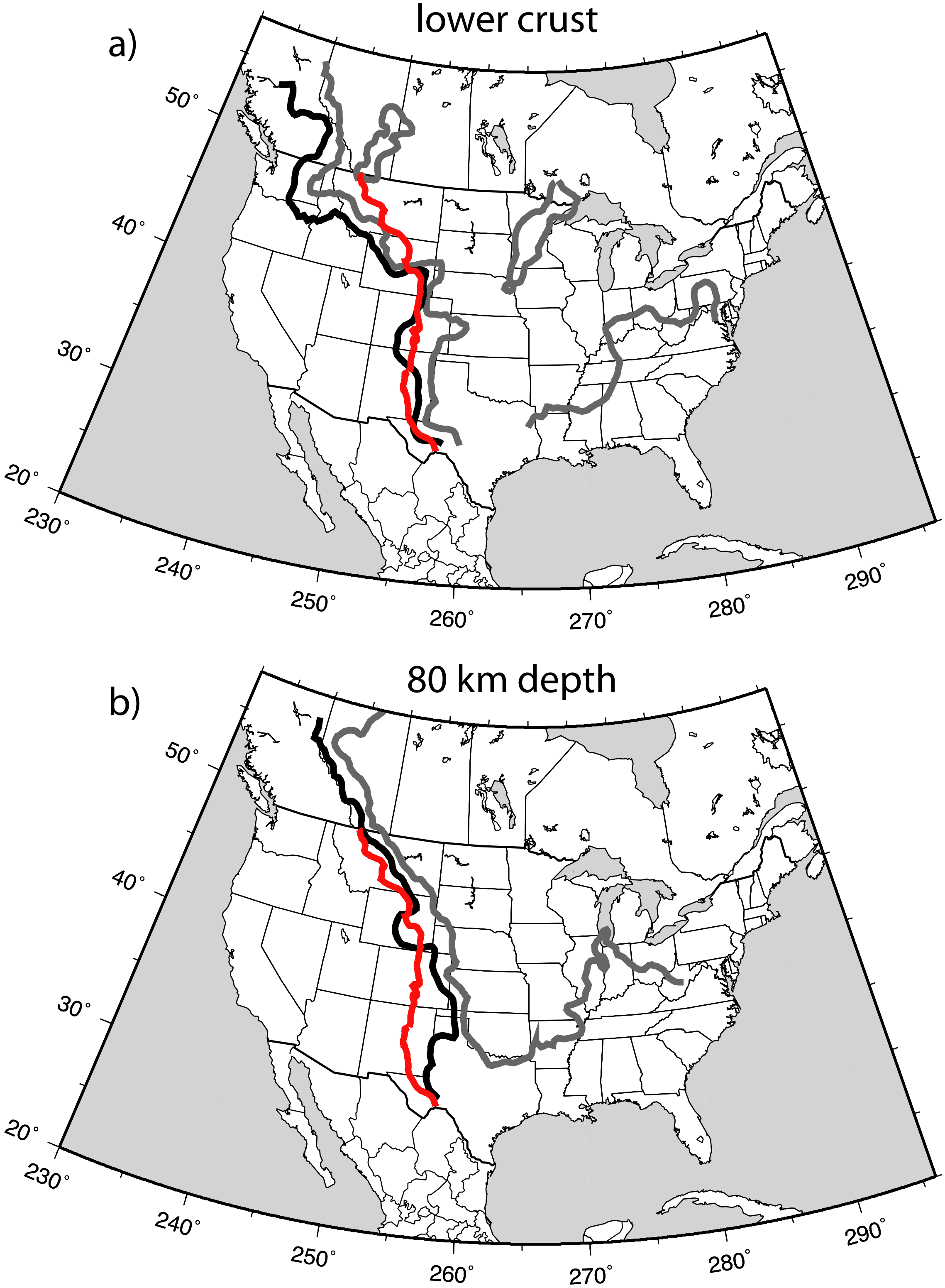
a)
lower crust
50°
40°
30°
20°
230°
240°
250°
260°
270°
280°
290°
b)
80 km depth
50°
40°
30°
20°
230°
240°
250°
260°
270°
280°
290°

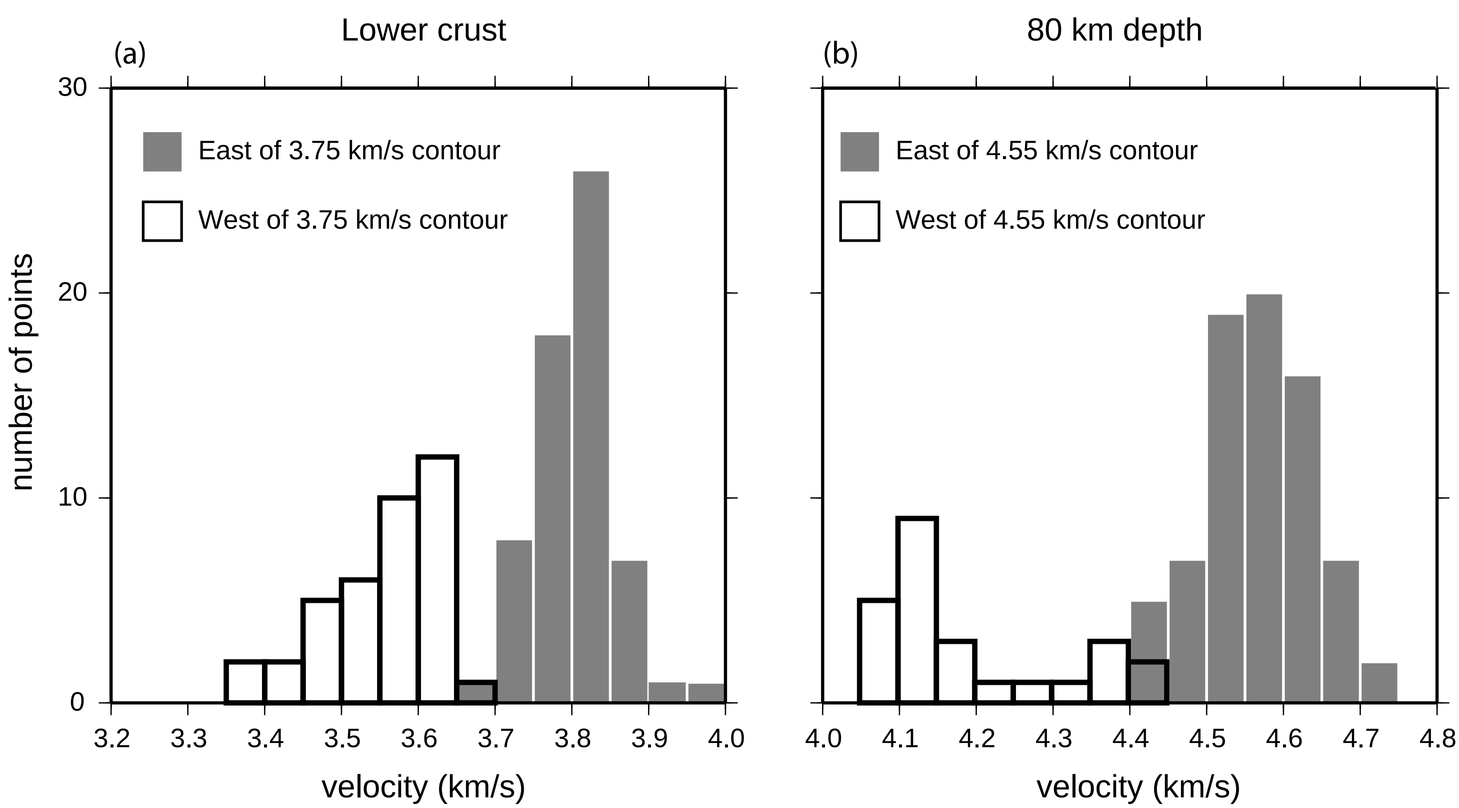

Lower crust
(a)
East of 3.75 km/s contour
West of 3.75 km/s contour
number of points
velocity (km/s)
80 km depth
(b)
East of 4.55 km/s contour
West of 4.55 km/s contour
velocity (km/s)

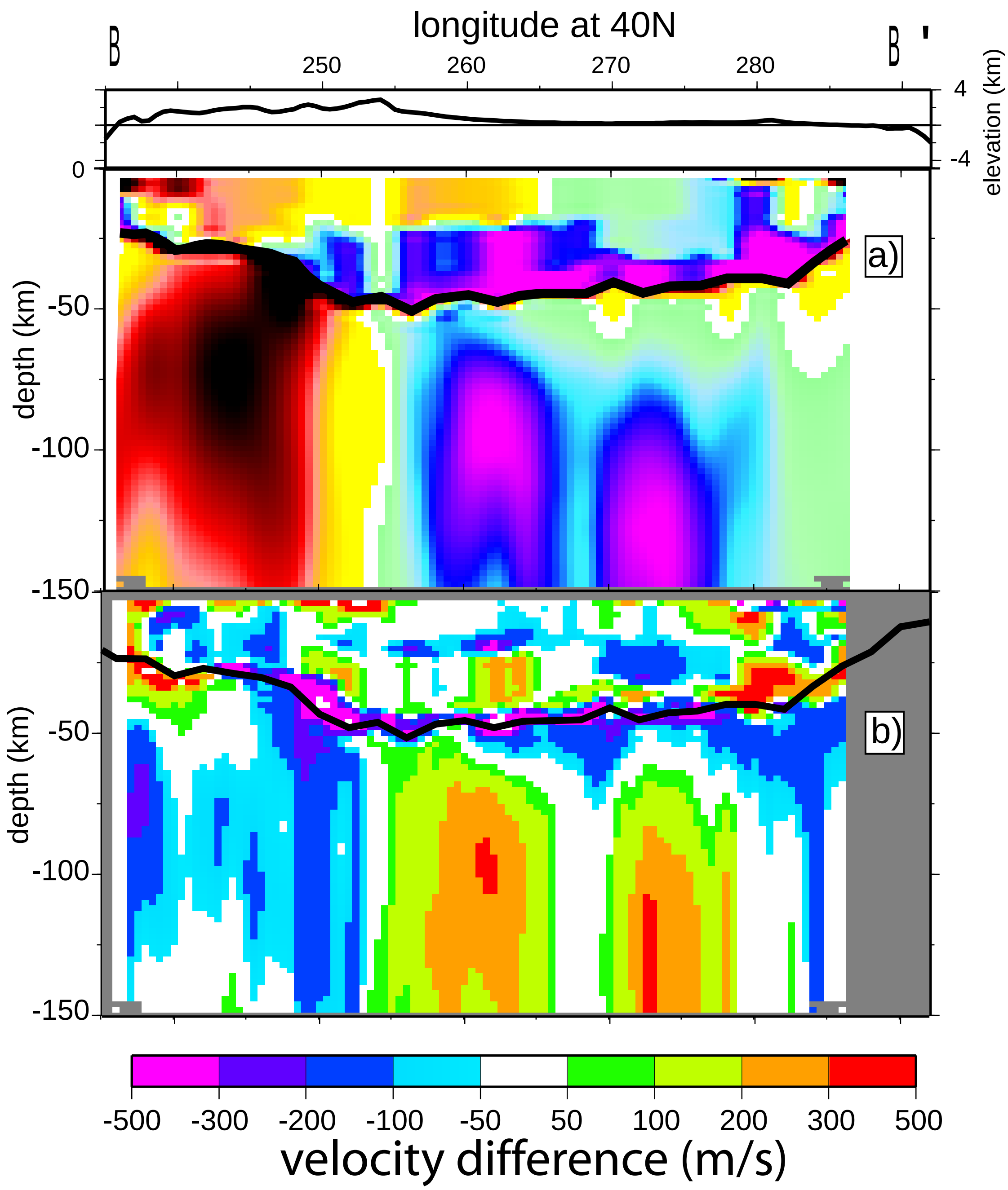

longitude at 40N
B
B '
250
260
270
280
4
-4
elevation (km)
0
-50
-100
-150
depth (km)
a)
b)
-500
-300
-200
-100
-50
50
100
200
300
500
velocity difference (m/s)

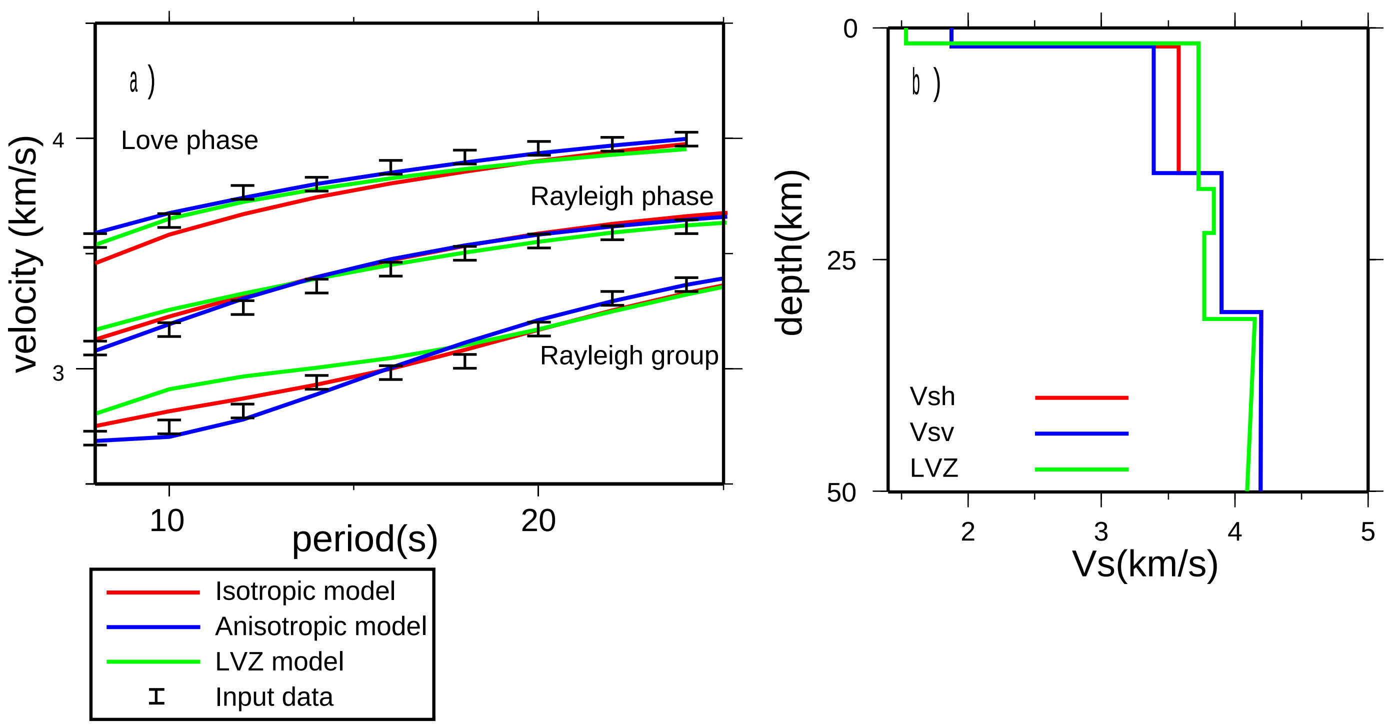

a)
Love phase
Rayleigh phase
Rayleigh group
velocity (km/s)
period(s)
4
3
10
20
Isotropic model
Anisotropic model
LVZ model
Input data
b)
depth(km)
Vs(km/s)
0
25
50
2
3
4
5
Vsh
Vsv
LVZ

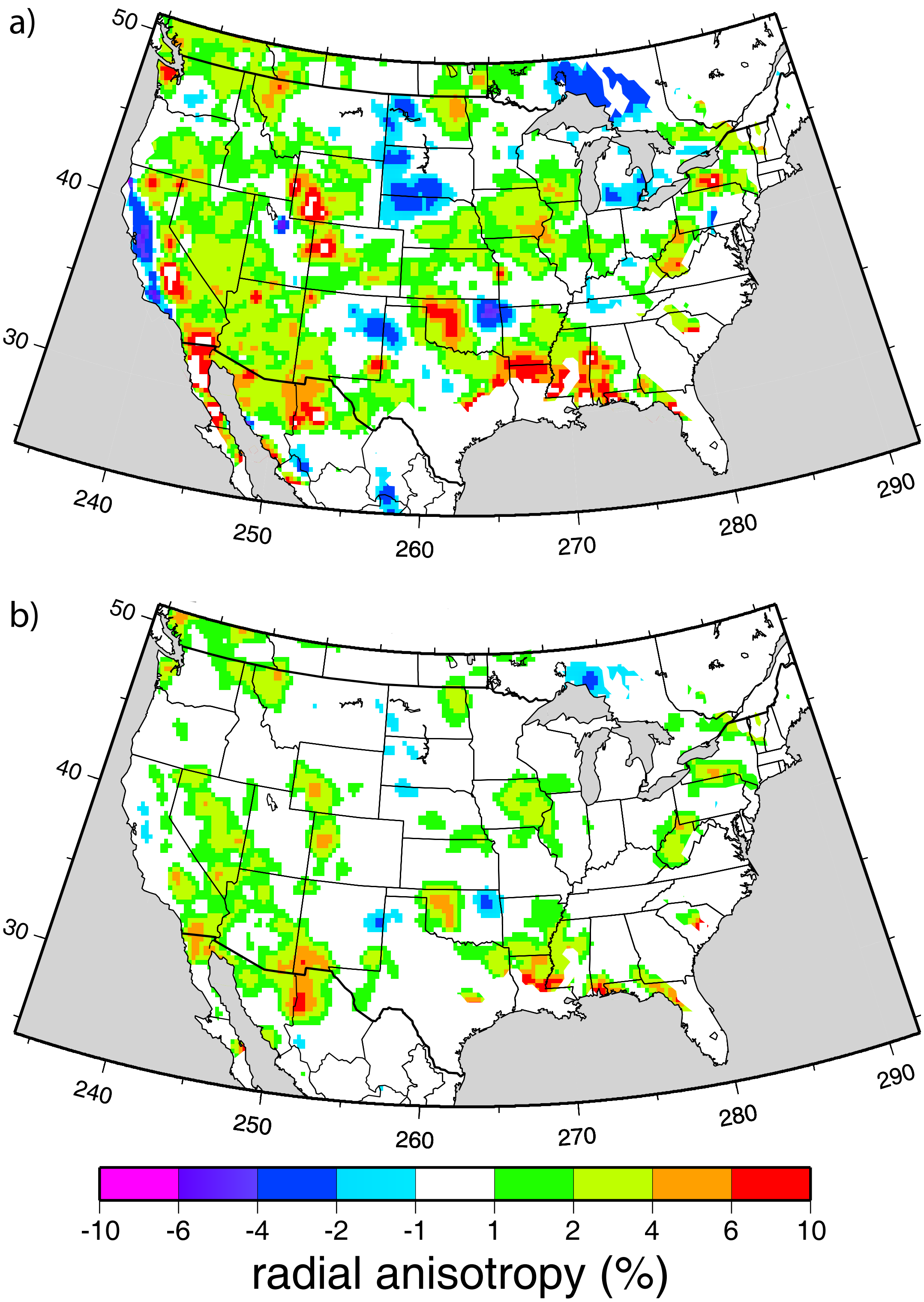
a)
50
40
30
240
250
260
270
280
290
b)
50
40
30
240
250
260
270
280
290
-10
-6
-4
-2
-1
1
2
4
6
10
radial anisotropy (%)